



# Hydrogel-Embedded Poly(Lactic-co-Glycolic Acid) Microspheres for the Delivery of hMSC-Derived Exosomes to Promote Bioactive Annulus Fibrosus Repair

Tyler J. DiStefano<sup>1</sup> , Keti Vaso<sup>2</sup>, Christopher J. Panebianco<sup>1</sup>, George Danias<sup>1</sup>, Henry N. Chionuma<sup>1</sup>, Kuriakose Kunnath<sup>3</sup>, Stylianos Z. Karoulias<sup>1</sup>, Minghui Wang<sup>4,5,6</sup>, Peng Xu<sup>4,5,6</sup>, Rajesh N. Davé<sup>3</sup>, Susmita Sahoo<sup>7</sup>, Jennifer R. Weiser<sup>2</sup>, and James C. Iatridis<sup>8</sup> 

## Abstract

**Objective.** Intervertebral disk degeneration is a prevalent postoperative complication after discectomy, underscoring the need to develop preventative and bioactive treatment strategies that decelerate degeneration and seal annulus fibrosus (AF) defects. Human mesenchymal stem cell–derived exosomes (MSC-Exos) hold promise for cell-free bioactive repair; however, their ability to promote AF repair is poorly understood. The objective of this study was to evaluate the ability of MSC-Exos to promote endogenous AF repair processes and integrate MSC-Exos within a biomaterial delivery system. **Design.** We characterize biophysical and biochemical properties of normoxic (Nx) and hypoxic (Hx) preconditioned MSC-Exos from young, healthy donors and examine their effects on AF cell proliferation, migration, and gene expression. We then integrate a poly(lactic-co-glycolic acid) microsphere (PLGA  $\mu$ Sphere) delivery platform within an interpenetrating network hydrogel to facilitate sustained MSC-Exo delivery. **Results.** Hx MSC-Exos led to a more robust response in AF cell proliferation and migration than Nx MSC-Exos and was selected for a downstream protection experiment. Hx MSC-Exos maintained a healthy AF cell phenotype under a TNF $\alpha$  challenge *in vitro* and attenuated catabolic responses. In all functional assays, AF cell responses were more sensitive to Hx MSC-Exos than Nx MSC-Exos. PLGA  $\mu$ Spheres released MSC-Exos over a clinically relevant timescale without affecting hydrogel modulus or pH upon initial embedment and  $\mu$ Sphere degradation. **Conclusions.** This MSC-Exo treatment strategy may offer benefits of stem cell therapy without the need for exogenous stem cell transplantation by stimulating cell proliferation, promoting cell migration, and protecting cells from the degenerative proinflammatory microenvironment.

## Keywords

intervertebral disk, hydrogels, extracellular vesicles, exosomes, drug delivery

## Introduction

Lesions in the annulus fibrosus (AF) are a significant risk factor for intervertebral disk (IVD) herniation, biomechanical dysfunction, and progressive degeneration, yet current discectomy procedures do not repair AF defects after nerve root decompression.<sup>1–4</sup> Since the IVD is the largest avascular organ in the body, it has a poor intrinsic healing capacity and AF defects tend to heal by the formation of a fibrous capsule at the outer AF.<sup>5–8</sup> These poor healing outcomes can lead to painful postoperative complications following discectomy such as recurrent herniation and progressive IVD degeneration (IVDD), thus motivating development of

strategies that improve repair of AF defects to slow IVDD and mitigate the risk of adverse events after surgery.<sup>9–13</sup>

Injectable bioadhesive hydrogels are an emerging treatment option to seal AF defects and prevent recurrent herniation of nucleus pulposus (NP) tissue. Our group recently developed a 2-part biomaterial repair strategy composed of a dual-modified glycosaminoglycan that bonds an interpenetrating network (IPN) hydrogel to extracellular matrix proteins to seals AF defects.<sup>14</sup> The low modulus hydrogel had low herniation risk and may be amenable for delivery of bioactive agents. Regenerative strategies that promote AF repair using exogenous cell delivery is challenging because of low cell viability, injectate leakage, aberrant differentiation, and



osteophyte formation.<sup>15-22</sup> The development of cell-free alternatives that can overcome these translational obstacles and prevent progressive IVDD.<sup>23-27</sup> Furthermore, its delivery in a biomaterial sealant also has potential to provide functional repair.

Mesenchymal stem cell-derived exosomes (MSC-Exos) are an emerging cell-free strategy with demonstrated potential to promote endogenous tissue repair for a number of tissues.<sup>28-31</sup> Specifically, MSC-Exos enhanced healing outcomes by attenuating inflammation, reducing catabolism, decreasing levels of apoptosis, promoting proliferation, and stimulating migration.<sup>28,29,32,33</sup> The use of MSC-Exos to treat IVDD is still in its infancy, with few prior studies targeting IVDD. Studies that do use MSC-Exos for IVDD focus on NP or organ-level responses to treatment with a dearth of information regarding AF responses to treatment.<sup>34-43</sup> Given the distinct differences between AF and NP phenotypes, as well as their functional roles in IVD homeostasis and healing, there is a clear need to define AF cell treatment responses to MSC-Exos in order to evaluate their regenerative potential for cell-free therapy in a tissue-specific manner.<sup>44-46</sup>

Two important considerations for the success of MSC-Exo therapy are the specific bioactive cargo and the delivery system. Few studies have demonstrated regulatory effects of the parent cell's culture environment on the MSC-Exos molecular signature which may be implicated in MSC-Exo treatment responses.<sup>47</sup> Particularly, the oxygen tension ( $pO_2$ ) of MSC culture may differentially regulate specific small RNA transcripts.<sup>48-50</sup> Therefore, normoxic (Nx; 18.6%  $O_2$ ) and hypoxic (Hx; 5%  $O_2$ ) MSC culture conditions were used to determine the influence of  $pO_2$  on the composition of human MSC-Exos. In regard to the delivery system, poly(lactic-co-glycolic acid) (PLGA) is a Food and Drug Administration (FDA)-approved biodegradable, biocompatible synthetic copolymer that is widely used to fabricate microsphere carriers (PLGA  $\mu$ Spheres) for controlled release applications.<sup>51</sup> PLGA  $\mu$ Spheres loaded with MSC-Exos may be integrated into our IPN hydrogel to form a

bioactive AF sealant given that they achieve the following design goals: (1) incorporation of PLGA  $\mu$ Spheres does not significantly stiffen hydrogel constructs since the IVD herniation risk was shown to be inversely proportional to the hydrogel stiffness<sup>14</sup>; (2) degradation of PLGA  $\mu$ Spheres does not significantly decrease the environmental pH to that which aligns with the degenerative microenvironment since PLGA hydrolytically degrades into 2 acidic compounds and the acidic milieu can promote progressive degeneration<sup>20,52-54</sup>; and (3) PLGA  $\mu$ Spheres demonstrate proof-of-concept encapsulation and subsequent release of MSC-Exos on a clinically relevant timescale in order to postoperatively enhance endogenous AF repair responses.

The global objectives of this study are 2-fold: (1) to evaluate the therapeutic potential of MSC-Exos to enhance endogenous AF repair and prevent hallmarks of IVDD *in vitro* and (2) integrate a biodegradable MSC-Exo carrier for local delivery to the AF (**Fig. 1**). In Part 1, we compare the biophysical and biochemical composition between Nx and Hx preconditioned MSC-Exos, then assess migratory and proliferative AF cell responses to MSC-Exo treatment in order to select the MSC  $pO_2$  conditioning environment with the most robust responses. We next apply this MSC-Exo group to TNF $\alpha$ -challenged AF cells to determine whether MSC-Exos can enable AF cells to resist aberrant changes in cell phenotype under a proinflammatory cytokine challenge. In Part 2, we integrate a degradable PLGA  $\mu$ Sphere carrier within an adhesive hydrogel system for the local delivery of MSC-Exos to AF repair sites. We evaluate the effects of PLGA  $\mu$ Sphere embedment on the short- and long-term mechanical and material properties of the hydrogel, assess the effect of PLGA degradation on culture acidity, and determine whether PLGA  $\mu$ Spheres can feasibly encapsulate MSC-Exos and enable sustained release. Successful completion of Parts 1 and 2 will demonstrate proof-of-concept that IPN hydrogel-embedded PLGA  $\mu$ Spheres loaded with MSC-Exos can be used to engineer a bioactive AF sealant for treating IVDD.

---

<sup>1</sup>Leni and Peter W. May Department of Orthopaedics, Icahn School of Medicine at Mount Sinai, New York, NY, USA

<sup>2</sup>Department of Chemical Engineering, The Cooper Union for the Advancement of Science and Art, New York, NY, USA

<sup>3</sup>Department of Chemical Engineering, New Jersey Institute of Technology, Newark, NJ, USA

<sup>4</sup>Department of Genetics and Genomic Sciences, Icahn School of Medicine at Mount Sinai, New York, NY, USA

<sup>5</sup>Mount Sinai Center for Transformative Disease Modeling, Icahn School of Medicine at Mount Sinai, New York, NY, USA

<sup>6</sup>Icahn Institute for Data Science and Genomic Technology, Icahn School of Medicine at Mount Sinai, New York, NY, USA

<sup>7</sup>Cardiovascular Research Center, Icahn School of Medicine at Mount Sinai, New York, NY, USA

<sup>8</sup>Orthopaedic Research Laboratories, Leni and Peter W. May Department of Orthopaedics, Icahn School of Medicine at Mount Sinai, New York, NY, USA

#### Corresponding Author:

James C. Iatridis, Orthopaedic Research Laboratories, Leni and Peter W. May Department of Orthopaedics, Icahn School of Medicine at Mount Sinai, 1 Gustave L. Levy Place, Box 1188, New York, NY 10029, USA.

Email: james.iatridis@mssm.edu

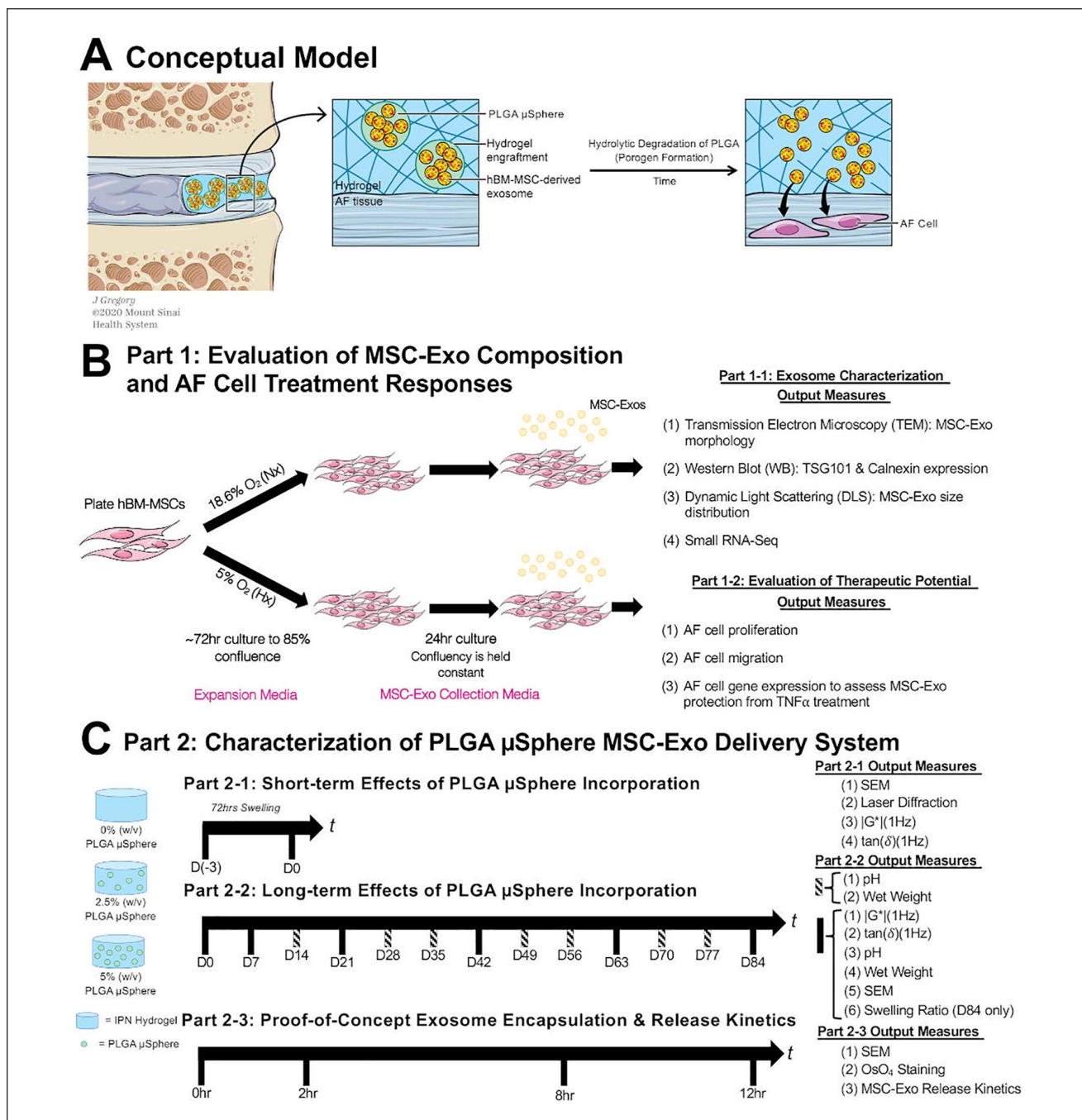


**Figure 1.** Conceptual model of the bioactive AF repair strategy and 2-part study design. **(A)** Conceptual model of MSC-Exo-laden IPN hydrogel for cell-free AF repair. **(B)** Part I study design for MSC-Exo characterization and AF cell treatment. **(C)** Part 2 study design to characterize MSC-Exo delivery system. AF = annulus fibrosus; MSC-Exo = mesenchymal stem cell-derived exosome; IPN = interpenetrating network; PLGA = poly(lactic-co-glycolic acid); hBM = human bone marrow; SEM = scanning electron microscopy.

## Materials and Methods

### *hBM-MSC Culture for MSC-Exo Production*

Human Bone Marrow-MSCs (hBM-MSCs) from 3 young, healthy biological donors (MSC00115, MSC00175, and

MSC00179) were purchased from RoosterBio Inc., Frederick, MD. MSC donor selection criteria included young adult age, high positivity for CD166, CD105, CD90, and CD73 flow markers, and negative for CD14, CD34, and CD45 flow markers. hBM-MSCs from donor MSC00115,

MSC00175, and MSC00179 were isolated from a 20-year-old female, a 25-year-old male, and a 21-year-old male, respectively. hBM-MSCs for all donors were demonstrated to have trilineage (adipogenic, osteogenic, and chondrogenic) differentiation potential from the supplier. Frozen hBM-MSCs (RoosterVial™-hBM-10M) were thawed and spun down to remove excess dimethyl sulfoxide (DMSO) in the freezing medium, then cultured using tissue culture treated Corning® CellSTACK® CS2 culture chambers (Corning Inc., Kennebunk, ME). hBM-MSCs were cultured in either normoxic (18.6% O<sub>2</sub>, 5% CO<sub>2</sub>, 70.2% N<sub>2</sub>) conditions or hypoxic conditions (5% O<sub>2</sub>, 5% CO<sub>2</sub>, 83.8% N<sub>2</sub>) at 37 °C for expansion according to supplier's instructions.

At 90% confluency, hBM-MSC expansion culture medium was aspirated and fully exchanged with RoosterCollect™-EV medium supplemented with of EV Boost™. After 24 hours, the MSC-conditioned medium was collected and stored at -80 °C until downstream use for MSC-Exo isolation. Of note, hypoxic conditioned hBM-MSCs remained in the hypoxic incubator, undisturbed for the full expansion phase (~72 h) as well as the MSC-Exo conditioning phase (~24 h), with the exception to exchange media after confluency was reached (~5 min).<sup>55</sup>

### *MSC-Exo Isolation from MSC Conditioned Medium*

MSC-Exos were isolated from conditioned media by ultracentrifugation and separated from the soluble protein fraction using a sucrose gradient, as previously described.<sup>56</sup> The Micro BCA™ Protein Assay Kit (Thermo Fisher Scientific, Rochester, NY) was used according to manufacturer's instructions to quantify MSC-Exo concentration in all freshly isolated samples and then immediately stored at -80 °C until downstream use.

### *Transmission Electron Microscopy*

Isolated MSC-Exos were characterized by transmission electron microscopy (TEM) to examine MSC-Exo morphology. MSC-Exos samples were first fixed in 2% paraformaldehyde (PFA; Electron Microscopy Sciences, Hatfield, PA) for 5 minutes and subsequently loaded on copper grids (Electron Microscopy Sciences) to air dry for 10 minutes. After drying, 1% uranyl acetate solution was applied to the sample for at least 10 minutes for negative staining. Samples were then imaged at 80 kV and 25,000x magnification on a HT7000 transmission electron microscope (Hitachi America, Ltd., Santa Clara, CA).

### *Dynamic Light Scattering*

Isolated MSC-Exos were characterized by dynamic light scattering (DLS) to determine nanoparticle size distribution.

About 30 µL of reconstituted MSC-Exos was added to 970 µL of 1X phosphate-buffered saline (PBS) in a spectrophotometry cuvette (Fisher Scientific, Fair Lawn, NJ). The cuvette was placed in the ZetaPALS Zeta Potential Analyzer and data were acquired over 3 cycles (1.5 min/cycle) and analyzed using ZetaPALS Particle Sizing Software (Brookhaven Instruments Corporation, Holtsville, NY). Lognormal size distributions for each sample were exported and the D<sub>50</sub> values for hydrodynamic diameters were recorded.

### *MSC-Exo Protein Extraction and Western Blot*

Following ultracentrifugation, MSC-Exos were lysed directly in 1x Pierce™ RIPA Lysis and Extraction Buffer (Thermo Fisher Scientific) at 4 °C. After collection, protein expression in MSC-Exos was analyzed by western blot, as previously described.<sup>56,57</sup> The 2 primary antibodies were used to examine protein expression in MSC-Exo samples and hMSC lysate controls: Mouse monoclonal antibody [4A10] to human TSG101 (ab83, 1:1000, Abcam Inc., Cambridge, MA) and rabbit polyclonal antibody to human Calnexin (ab22595, 1:1000, Abcam Inc.).<sup>58</sup> IRDye® goat-*anti*-mouse or IRDye® goat-*anti*-rabbit were used as secondary antibodies (1:10,000 in 5% [w/v] non-fat milk in TBS-T, Jackson ImmunoResearch Laboratories, West Grove, PA). Polyvinylidene difluoride (PVDF) membranes were imaged using the Azure c600 Gel Imaging System (Azure Biosystems, Dublin, CA).

### *MSC-Exo RNA Isolation and Small RNA-Seq*

Following ultracentrifugation, MSC-Exos were collected directly in 500 µL of QIAzol Lysis Reagent (QIAGEN Sciences, Germantown, MD). After collection, samples were transferred into sterile 1.5 mL microcentrifuge tubes and total MSC-Exo RNA was isolated using a guanidinium thiocyanate-phenol-chloroform extraction method.<sup>59</sup> MSC-Exo RNA concentration was quantified using a Qubit® RNA High Sensitivity Assay Kit (Invitrogen, Carlsbad, CA) according to the manufacturer's instructions with a Qubit® 4 Fluorometer (Invitrogen). Samples were stored at -80 °C until downstream use for sequencing.

Sequencing was performed on an Illumina NextSeq 500 platform (Illumina, San Diego, CA) with NextSeq 500/550 High Output Kit V2 (Illumina) as the sequencing platform reagent. Norgen Biotek Small RNA Library Prep Kit was used for library preparation (Norgen Biotek Inc., Thorold, ON, Canada). miRbase version 21, gtRNadb, RNadb, Gencode version 21 (hg38) were used as reference/database sequences for miRs, tRNAs, piRNA, and genome species, respectively. Read counts of RNAs were first normalized using the trimmed mean of M-values normalization (TMM) method to adjust for sequencing library size difference.<sup>60</sup> To test whether any miRNAs were differentially expressed

between Hx and Nx MSC-Exo samples, paired differential expression analysis was performed by employing a moderated *t* test implemented in the limma package.<sup>61</sup>

### Primary AF Cell Isolation

Primary bovine AF cells were isolated from 10 healthy and skeletally mature biological donors from coccygeal levels cc1/2, cc2/3, cc3/4, and cc4/5 using a collagenase digestion protocol as previously described.<sup>14</sup> All primary AF cells were expanded to passage 2 (p2) in complete growth medium and cryopreserved in 93% (v/v) fetal bovine serum (FBS; Gemini Bio-Products, West Sacramento, CA) and 7% (v/v) DMSO (Sigma-Aldrich Inc., St. Louis, MO) as freezing medium. Complete growth medium was composed of high glucose (4.5g/L) DMEM (Life Technologies Corporation, Grand Island, NY), 10% fetal bovine serum (Gemini Bio-Products), 1% penicillin/streptomycin (Life Technologies Corporation), and 0.2% L-ascorbic acid (Fisher Scientific).

### Cell Proliferation Assay

AF cell proliferation was measured using the CellTiter-Glo® 2.0 Assay (Promega Corporation, Madison, WI) according to the manufacturer's instructions. Bovine AF cells (p2) from 3 biological donors were plated into Nunc™ MicroWell™ 96-Well Optical Bottom Plates with Polymer Base (Thermo Fisher Scientific) at a density of 4,000 cells/cm<sup>2</sup>. At the time of plating, cells were treated with 0 to 50 µg/mL of Nx or Hx MSC-Exos in serum-free medium from donors MSC00115, MSC00175, and MSC00179. All conditions were carried out in triplicate for all biological donors. Plates were cultured at 37 °C, 5% CO<sub>2</sub> until an assay timepoint was reached (0, 24, 48, and 72 h), then the CellTiter-Glo® 2.0 Assay was carried out. Luminescence in Relative Luminescence Units (RLUs) was recorded on a SpectraMax i3x Multi-Mode Microplate Reader (Molecular Devices, San Jose, CA). All RLU values were normalized to the untreated control values at each timepoint.

### Transwell Migration Assay

AF cell migration was evaluated using a Corning™ Transwell™ Multiple Well Plate with Permeable Polyester Membrane Inserts (8 µm pore size) (Corning Inc.) and adapted from a previously established protocol.<sup>62</sup> Bovine AF cells (p2) were first seeded on the top of the filter membrane and experimental medium was placed carefully into the bottom of the lower chamber according to following conditions: (1) serum-free medium (negative control), (2) serum-free medium supplemented with 100 ng/mL recombinant human CCL5/RANTES as a comparison group (Cat. No. 278-RN-010/CF; R&D Systems Inc., Minneapolis,

MN), and (3) serum-free medium supplemented with 50 µg/mL MSC-Exos. The well plate was then incubated at 37 °C, 5% CO<sub>2</sub> for 24 hours. After fixation with 4% paraformaldehyde at 4 °C for 15 minutes to fix migrated cells on the bottom side of the membrane, 0.2% (w/v) crystal violet (Sigma-Aldrich) was used to stain cells for 5 minutes. Transwell membranes were imaged on a Leica DM6 B (Leica Microsystems Inc., Buffalo Grove, IL). AF cell migration was evaluated for 3 biological donors in triplicate per condition. Migrated cells were counted using ImageJ software (National Institutes of Health, Bethesda, MD) and cell counts were normalized to the negative control conditions.

### Fluorescent Labeling of MSC-Exos and Uptake Visualization

MSC-Exos were labeled using the PKH67 Green Fluorescent Cell Linker Kit for General Cell Membrane Labeling (Sigma-Aldrich) according to the manufacturer's instructions. After preparation, samples were then centrifuged at 190,000 g for 2 hours at 4 °C. Following ultracentrifugation, the medium and interface layer was aspirated out and the fluorescently labeled MSC-Exo pellet was resuspended in sterile 1X PBS.

Bovine AF cells (p2) were plated in a Corning® Costar® 6-well Clear TC-Treated Multiple Well Plate (Corning Inc.) at a seeding density of 4000 cells/cm<sup>2</sup> in complete growth medium (2 mL/well). When 65% confluence was reached, complete growth medium was fully exchanged with serum-free medium for the following 2 conditions: (1) untreated serum-free medium and (2) serum-free medium supplemented with the total resuspended volume of fluorescently labeled MSC-Exos. Plates were incubated at 37 °C, 5% CO<sub>2</sub> for 6 hours. Following the 6-hour incubation period, AF cells were fixed with ice cold 4% PFA (Electron Microscopy Sciences) for 15 minutes, washed twice with 1X PBS (5 min/wash), and immediately imaged on a Leica DMi8 widefield microscope (Leica Microsystems Inc.).

### AF Cell Protection Experiment

AF cells (p2) from 10 biological bovine donors were plated in Corning® Costar® 12-well Clear TC-treated Multiple Well Plates at a density of 4,000 cells/cm<sup>2</sup> in complete growth medium (1 mL/well). When 85% confluence was reached, growth medium was aspirated and fully replaced with serum-free medium. Cells were divided into the following 5 groups: (1) serum-free medium (untreated control), (2) serum-free medium supplemented with 10 ng/mL recombinant human TNFα (Cat. No. 210-TA-020/CF; R&D Systems Inc.), (3-5) serum-free medium pre-treated with 50 µg/mL Hx MSC-Exos from donors MSC00115, MSC00175, or MSC00179 for 1 hour and subsequently

**Table 1.** Oligonucleotide Primers for Bovine Annulus Fibrosus Cell qPCR.

Gene Name	Gene Symbol	Sequence (5'-3')
Collagen, type I, alpha 1	COL1A1 (FWD)	CTGGGTACCACCGTTGATAGTTT
	COL1A1 (REV)	AGTCAAGAAGTGGTACAGAAATTC
Collagen, type II, alpha 1	COL2A1 (FWD)	TGATCGAGTACCGGTCACAGAA
	COL2A1 (REV)	CCATGGGTGCAATGTCAATG
Aggrecan	ACAN (FWD)	ACCTACGATGTCTACTGCTACG
	ACAN (REV)	AGAGTGGCGTTTTGGGATTC
Scleraxis	SCX (FWD)	CAGAGAAAGTTGGGCTCAGGG
	SCX (REV)	GGGGGCTGTCGTCTTCCCTC
Mohawk	MKX (FWD)	AAAGGGACCAGCAAGGATG
	MKX (REV)	ACCGTCTTCACTTCCGCAAT
Matrix metalloproteinase-1	MMP1 (FWD)	TTCAACCAGGTGCAGGTATC
	MMP1 (REV)	AGCCCCAATGTCAGTAGAATG
Interleukin 6	IL6 (FWD)	GGGAAATCAGGAAAATGTCAGG
	IL6 (REV)	TTACCCACTCGTTTTGAAGACTG
NLR family pyrin domain containing 3	NLRP3 (FWD)	GGGACTGAGGCATCTATTCTG
	NLRP3 (REV)	GAGTCTCCCAGAGCATTTTCC
Glyceraldehyde 3-phosphate dehydrogenase	GAPDH (FWD)	CACCCACGGCAAGTTCAAC
	GAPDH (REV)	TCTCGCTCCTGGAAGATGGT

supplemented with 10 ng/mL recombinant human TNF $\alpha$ . Cells were incubated at 37 °C, 5% CO<sub>2</sub> for 24 hours.

### RNA Isolation and Quantitative Real-Time Polymerase Chain Reaction

Following the protection experiment incubation period, AF cell RNA was isolated by guanidinium thiocyanate-phenol-chloroform extraction with TRIzol™ Reagent (Life Technologies Corporation), as described (“MSC-Exo RNA Isolation & Small RNA-Seq” section). cDNA was synthesized with 1  $\mu$ g of total RNA from each sample using a High Capacity cDNA Reverse Transcription Kit (Applied Biosystems, Foster City, CA) according to the manufacturer’s instructions. Gene expression was determined using quantitative real-time polymerase chain reaction (qRT-PCR). An ABI PRISM® 7900HT Sequence Detection System (Applied Biosystems) was used to determine cycles to amplification for qRT-PCR reactions with Power SYBR™ Green PCR Master Mix (Applied Biosystems), according to manufacturer’s instructions. Specific primer sequences for genes of interest can be found in **Table 1**. Fold changes in gene expression were determined using the 2<sup>- $\Delta\Delta$ Ct</sup> quantification method.

### PLGA $\mu$ Sphere Fabrication

Blank and exosome-loaded PLGA  $\mu$ Spheres were fabricated with poly(D,L-lactide-co-glycolide) (PLGA; 75:25 lactide: glycolide; M<sub>w</sub> = 66-107 kDa; Sigma-Aldrich) using a modified double emulsion technique.<sup>63</sup> For exosome-loaded  $\mu$ Spheres, 125  $\mu$ L of isolated MSC-Exos in 1X PBS was added to the primary emulsion and subsequently vortexed

on high speed for 5 seconds. About 5 mL of 4% (w/v) poly(vinyl alcohol) (PVA; M<sub>w</sub> = 31-50 kDa; 98-99% hydrolyzed; Sigma-Aldrich) was then added to the solution to form the second emulsion (w/o/w) and the second emulsion was vortexed for either 15 seconds ( $\mu$ Sphere Condition 1), 30 seconds ( $\mu$ Sphere Condition 2), 45 seconds ( $\mu$ Sphere Condition 3), or 60 seconds ( $\mu$ Sphere Condition 4). Following collection, PLGA  $\mu$ Spheres were frozen down at -80 °C overnight and subsequently lyophilized for 7 days to obtain freeze-dried  $\mu$ Sphere product.

### PLGA $\mu$ Sphere Particle Size Distribution Analysis

Particle size distribution (PSD) was measured for all  $\mu$ Sphere conditions by laser diffraction with dynamic image analysis using a RODOS-Helos system (Sympatec Inc., Pennington, NJ) at an operating pressure of 0.5 bar. Following data acquisition, the D<sub>10</sub> (10<sup>th</sup> percentile), D<sub>50</sub> (50<sup>th</sup> percentile), and D<sub>90</sub> (90<sup>th</sup> percentile) diameter values were recorded for each PLGA  $\mu$ Sphere condition in triplicate batches.

### IPN Hydrogel Fabrication

About 15% (v/v) poly(ethylene glycol) diacrylate (PEGDA; M<sub>w</sub> = 20 kDa; Polysciences Inc., Warrington, PA) IPN hydrogels were fabricated as previously described.<sup>14</sup> Hydrogels for the short-term and long-term studies (Parts 2-1 and 2-2) incorporated blank PLGA  $\mu$ Spheres in the prepolymer solution at 2.5% (w/v) and 5% (w/v). Hydrogels for the release kinetics experiment (Part 2-3) incorporated MSC-Exo-laden PLGA  $\mu$ Spheres in the prepolymer solution at 2.5% (w/v) and 5% (w/v).

### Scanning Electron Microscopy

Scanning electron microscopy (SEM) imaging was performed on a Hitachi S-4300 system (Hitachi America, Ltd.). All samples were prepared by lyophilization for 7 days and subsequently sputter coated with gold-palladium (Electron Microscopy Sciences) for 2 cycles. SEM images were taken at 2 to 5 kV to ensure that samples would not charge during image acquisition. Pore size and PLGA  $\mu$ Sphere counts were quantified from independent technical replicates ( $N = 4$ -5/group) over the 84-day culture period. Hydrogel pore size measurements are reported as the largest pore diameter(s) for each discernable pore within 3 independent regions of interest (ROIs) for a given technical replicate. PLGA  $\mu$ Sphere count is reported as the mean number of visible  $\mu$ Spheres across 3 regions of interest for a given technical replicate.

### Hydrogel Mechanical Testing

Hydrogel specimens underwent parallel plate shear testing ( $N = 10$ /group) after a 72-hour swelling period in 1X PBS using a TA Instruments AR2000ex rheometer (TA Instruments, New Castle, DE) to evaluate short-term mechanical effects of  $\mu$ Sphere embedment on IPN hydrogels. To examine the long-term effects of  $\mu$ Sphere embedment on IPN hydrogel mechanical properties, the same mechanical testing protocol was performed on days 7, 21, 42, 63, and 84. Specimens underwent a frequency sweep from 0.1 to 10 Hz at 1% strain, and the complex modulus ( $|G^*|$ ) and tangent phase angle ( $\tan \delta$ ) values were obtained at 1 Hz, which is a physiologically relevant loading frequency.<sup>64</sup>

### pH Measurements

pH of solution was measured at the start of the 84-day culture period and every 7 days for each hydrogel in culture ( $N = 7$ -10/group/timepoint) using a FiveGo Portable F2 pH/mV Meter (Mettler-Toledo, Columbus, OH). Buffer was fully exchanged with sterile 1X PBS every 7 days and the pH of fresh buffer was measured before each exchange.

### Specimen Wet Weight and Swelling Ratio

Before placing specimens in new buffer for medium exchange, the wet weight of all hydrogel formulations ( $N = 17$ -20/group/timepoint) was recorded using a Sartorius CP124S Analytical Balance (Sartorius Corporation, Bohemia, NY). After 84 days of culture, the hydrogel specimens were lyophilized for 7 days and the dry weight was recorded. Using both the wet and dry weight measurements at the 84-day timepoint, the swelling ratio was calculated using the following equation:  $Q_w = M_{\text{wet}}/M_{\text{dry}}$ .

### Histological Assessment of PLGA $\mu$ Spheres

Lyophilized PLGA  $\mu$ Spheres with and without encapsulated MSC-Exos were first embedded in EpreDia™ HistoGel™ Specimen Processing Gel (EpreDia, Kalamazoo, MI) and then fixed in aqueous buffered zinc formalin fixative (Anatech Ltd., Battle Creek, MI) for 48 hours. After fixation, specimens were placed in a 4% osmium tetroxide ( $\text{OsO}_4$ ) solution (Electron Microscopy Sciences) for 2 hours to crosslink MSC-Exo lipids. Specimens were then infiltrated with a hydrophilic resin, 2-hydroxypropyl methacrylate (Sigma-Aldrich), for 48 hours with 2 changes of monomer solution. The monomer solution was then polymerized by the slow addition of heat at 37 °C to form blocks for sectioning. About 5  $\mu\text{m}$  histological sections were then prepared, deplasticized, and imaged using a 63X oil immersion objective on a Leica DM6B Upright Microscope (Leica Microsystems GmbH, Wetzlar, Germany).

### MSC-Exo Release Kinetics

MSC-Exo release kinetics for hydrogel-free  $\mu$ Spheres (i.e., PLGA  $\mu$ Spheres in 1X PBS) and hydrogel-embedded  $\mu$ Spheres (i.e., PLGA  $\mu$ Spheres in IPN hydrogels) was characterized by Nanoparticle Tracking Analysis (NTA) with a ZetaView® instrument (Particle Metrix Inc., Mebane, NC).<sup>65,66</sup> Samples were cultured in sterile 1X PBS, and culture medium was fully exchanged at collection timepoints and on a weekly basis. Releasate samples were collected at 0-, 2-, 8-, and 12-hour timepoints ( $N = 4$ /group/timepoint) for the following conditions: (1) 7.5 mg PLGA  $\mu$ Spheres in 1 mL sterile 1X PBS, (2) 15 mg PLGA  $\mu$ Spheres in 1 mL sterile 1X PBS, (3) 2.5% (w/v) PLGA  $\mu$ Spheres embedded in IPN hydrogels cultured with 3 mL sterile 1X PBS, and (4) 5% (w/v) PLGA  $\mu$ Spheres embedded in IPN hydrogels cultured with 3 mL sterile 1X PBS. About 7.5 mg PLGA  $\mu$ Spheres equates to the amount of  $\mu$ Spheres in one hydrogel-embedded technical replicate at 2.5% (w/v) and 15 mg PLGA  $\mu$ Spheres equates to the amount of  $\mu$ Spheres in one hydrogel-embedded technical replicate at 5% (w/v).

### Statistical Analyses

Quantitative data were reported as mean  $\pm$  standard deviation. Student's  $t$  test assessed effects of  $p\text{O}_2$  on MSC-Exo hydrodynamic diameter. Analysis of variance (ANOVA) with Tukey's *post hoc* tests assessed effects of PLGA concentration on hydrogel swelling ratio ( $Q_w$ ), and complex shear modulus ( $|G^*|$ ), and Brown-Forsythe and Welch ANOVA with Dunnett's T3 assessed tangent phase angle ( $\tan \delta$ ) due to unequal variance. Two-way ANOVA assessed quantitative data pertaining to AF cell proliferation response, AF cell migration, long-term  $|G^*|$  response, long-term  $\tan \delta$  response, hydrogel pore size measurements,

$\mu$ Sphere count measurements, and  $\mu$ Sphere diameter, and MSC-Exo release kinetics measurements. Dunnett's *post hoc* detected differences across groups in AF cell proliferation, long-term  $|G^*|$  response, long-term  $\tan \delta$  response, and MSC-Exo release kinetics. Tukey's *post hoc* was used to detect specific differences across groups in hydrogel pore size over time. Šidák's multiple comparison test detected differences across groups in AF cell migration. Mixed-effects analyses with Dunnett's multiple comparisons test was used to assess significant differences across groups for quantitative data pertaining to AF cell gene expression, pH, and hydrogel wet weight. ROUT method ( $Q = 1\%$ ) was used to remove outliers for qPCR gene expression analyses. AF cell proliferation response over time was plotted and fit via linear regression for a given MSC donor at  $50 \mu\text{g}/\text{mL}$  MSC-Exos and differences in regression coefficients across MSC-Exo  $\text{pO}_2$  groups were tested via *t* test. Pearson correlation evaluated the strength of association of AF cell proliferation with miR-21-5p read counts in MSC-Exo samples, and of AF cell migration with miR-652-3p and miR-214-5p read counts. Statistical analyses used GraphPad Prism 9 (GraphPad Software, San Diego, CA) with  $\alpha = 0.05$ .

## Results

### Biophysical and Biochemical Characterization of MSC-Exos

MSC-Exos displayed a characteristic vesicular morphology distinct of exosomes using TEM, where samples featured a cup-like shape with a distinguishable lipid bilayer (**Fig. 2A**). All MSC-Exo groups exhibited undetectable protein expression for Calnexin (90 kDa) and detectable protein expression for TSG101 (47 kDa), consistent with established positive and negative markers for exosomes, respectively (**Fig. 2B**). Nx and Hx MSC-Exos featured hydrodynamic diameters within the accepted range for exosomes (30–150 nm), where Nx MSC-Exos had an average diameter of  $113.3 \text{ nm} \pm 30.56 \text{ nm}$  and Hx MSC-Exos had an average diameter of  $88.6 \text{ nm} \pm 34.49 \text{ nm}$  with no significant difference between  $\text{pO}_2$  groups ( $P = 0.407$ ) (**Fig. 2C**). Small RNA-Seq analyses indicated that there was no differential expression observed between Nx and Hx MSC-Exo groups, although there was considerable heterogeneity observed among biological MSC donors as visualized in the heatmap for the top 60 variable miRs (**Fig. 2D**). Principal component analysis showed that MSC donor and  $\text{pO}_2$  conditions contributed to variability in MSC-Exo small RNAs.  $\text{pO}_2$  conditions contributed to the variability in MSC-Exo small RNAs for donor MSC00179, where Nx and Hx groups did not cluster together due to differences along dimension 2. However,  $\text{pO}_2$  conditions did not appear to drive variability in MSC-Exo small RNAs for donors MSC00115 and MSC00175, as Nx and Hx groups clustered together on the principal component analysis (PCA) plot.

Notably, variability between donors MSC00115 and MSC00175 was observed along dimension 2 as well as variability in donor MSC00179 Hx along dimension 1 (**Fig. 2E**). Volcano plot shows miRs trending toward differential regulation between Nx and Hx MSC-Exos, although no transcripts were significantly upregulated or downregulated between  $\text{pO}_2$  MSC-Exo group after false discovery rate correction. Top 5 miRs (by FC differences) trending toward upregulation were miR-210-3p, miR-376a-5p, miR-10399-5p, miR-210-5p, and miR-3163. Top 5 miRs trending toward downregulation were miR-1292-5p, miR-23a-5p, miR-146b-5p, miR-296-5p, and miR-769-3p (**Fig. 2F**).

### AF Cell Proliferation

AF cells exhibited a dose- and time-dependent proliferative response to Nx and Hx MSC-Exo treatment. A significant interaction between MSC-Exo concentration and time was observed for both MSC-Exo treatment groups, suggesting a possible non-linear dosing effect. *Post hoc* analyses were used to identify the MSC-Exo concentration that elicited a proliferative effect in the shortest amount of time for each MSC-Exo treatment group. Nx MSC-Exos induced proliferation as quickly as 48 hours post-treatment using  $6.25 \mu\text{g}/\text{mL}$  MSC-Exos ( $P = 0.0001$ ) and Hx MSC-Exos induced proliferation as quickly as 72 hours post-treatment using  $6.25 \mu\text{g}/\text{mL}$  MSC-Exos ( $P < 0.0001$ ) (**Fig. 3A**). Comparison between  $\text{pO}_2$  MSC-Exo groups indicate that Hx MSC-Exos elicited a stronger proliferative response in AF cells over the 72-hour treatment period (at  $50 \mu\text{g}/\text{mL}$ ) compared with Nx MSC-Exos (**Fig. 3B**). There was a strong positive ( $r = 0.763$ ) and significant ( $P = 0.0389$ ) correlation between normalized luminescence and MSC-Exo miR-21-5p reads per million (**Fig. 3C**).

### AF Cell Migration

After 24 hours of culture, crystal violet staining demonstrated observable AF cell migration in response to an MSC-Exo chemotactic gradient at  $50 \mu\text{g}/\text{mL}$ , with notable visual differences compared with the negative control group and CCL5-treated positive control comparison group (**Fig. 4A**). Quantification of migrated AF cells indicated a significant main effect of MSC-Exo treatment on migrated cell count ( $p_{\text{treatment}} < 0.0001$ ). However, there was no statistical effect of MSC-Exo  $\text{pO}_2$  group on AF cell migratory response ( $p_{\text{pO}_2} = 0.3818$ ). *Post hoc* analyses indicated a significant increase in migratory response compared with the negative control when a chemotactic gradient was established with  $50 \mu\text{g}/\text{mL}$  of Hx MSC-Exos ( $P = 0.0005$ ), but not for Nx MSC-Exos ( $P = 0.0629$ ). No statistical difference was observed in AF cell migration when a chemotactic gradient was established with CCL5 at  $100 \text{ ng}/\text{mL}$  ( $P = 0.8260$ ) (**Fig. 4B**). There was a strong negative ( $r = -0.796$ ) and significant ( $P = 0.0292$ ) correlation between normalized migrated cell count and



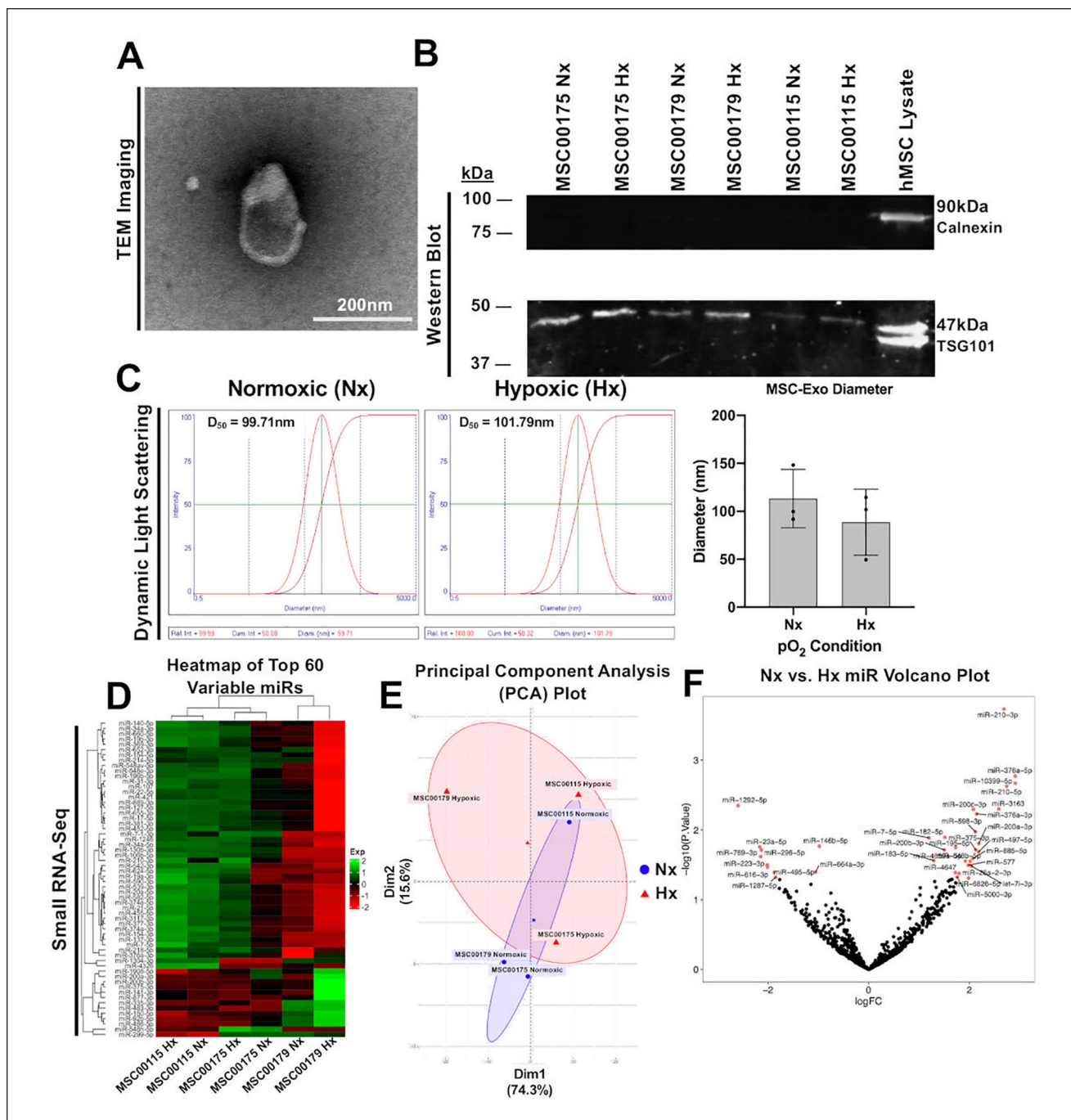


**Figure 2.** MSC-Exos exhibited biophysical and biochemical properties that align with established exosome properties, with no difference observed between pO<sub>2</sub> conditioning environments in MSC-Exo protein expression, hydrodynamic diameter, or small RNA-Seq analyses. **(A)** Representative transmission electron microscope image of an MSC-Exo following isolation. TEM magnification = 25 K; Scale bar = 200 nm. **(B)** Western blot of positive exosome marker TSG101 and negative exosome marker Calnexin. **(C)** Representative lognormal distributions of MSC-Exo hydrodynamic diameter obtained via dynamic light scattering, with no significant differences observed between Nx and Hx MSC-Exos. **(D)** Heatmap of the 60 miR transcripts with the highest observed variability across MSC-Exo groups. **(E)** Principal component analysis plot of the MSC-Exo groups using the 2 most variable dimensions. **(F)** Volcano plot of upregulated and downregulated miR transcripts. Transcripts labeled as red for nominal  $P < 0.05$  ( $P$  value before multiple-test correction). Y-axis =  $-\log_{10}(P_{\text{nominal}})$  and X-axis =  $\log_2(\text{Fold Change})$ . MSC-Exo = mesenchymal stem cell-derived exosome; TEM = transmission electron microscopy.

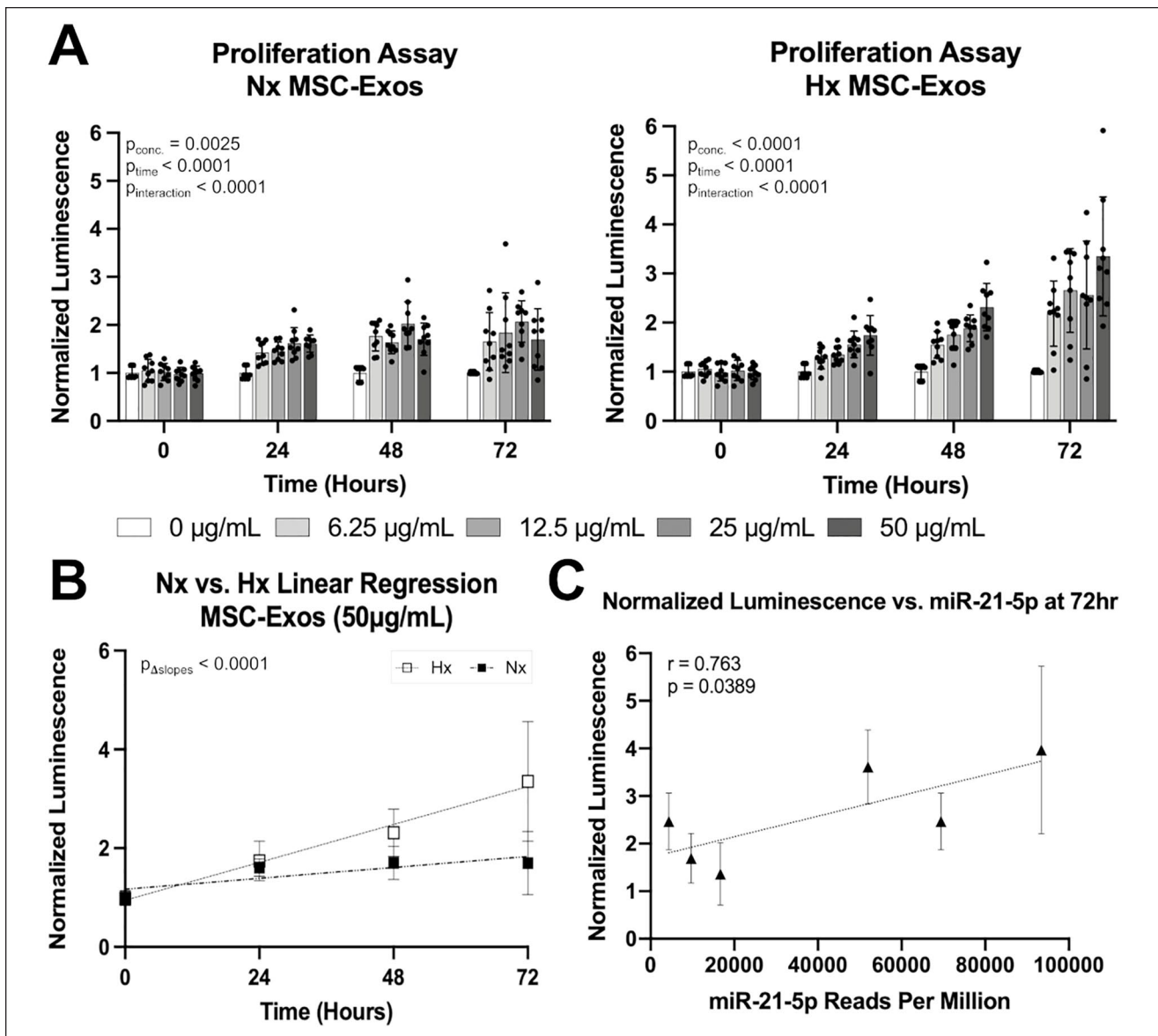


**Figure 3.** MSC-Exo treatment promotes AF cell proliferation over 72 hours in a dose-dependent manner with a more robust proliferative response to Hx MSC-Exos than Nx MSC-Exos. **(A)** Normalized luminescence readings from the CellTiter-Glo® 2.0 assay at 0, 24, 48, and 72 hours after Nx and Hx MSC-Exo treatment at 0, 6.25, 12.5, 25, and 50  $\mu\text{g/mL}$  showed significant increases with dose and time. **(B)** Hx MSC-Exo treatment had significantly greater proliferation than Nx MSC-Exo treatment. **(C)** Luminescence significantly correlated with MSC-Exo miR-21-5p reads per million 72 hours after treatment at 50  $\mu\text{g/mL}$ . MSC-Exo = mesenchymal stem cell-derived exosome; AF = annulus fibrosus.

MSC-Exo miR-652-3p reads per million (**Fig. 4C**). There was also a strong negative ( $r = -0.743$ ) and significant ( $P = 0.0453$ ) correlation between normalized migrated cell count and MSC-Exo miR-214-5p reads per million (**Fig. 4D**).

#### AF Cell Internalization of MSC-Exos

AF cells internalized MSC-Exos within 6 hours following treatment, as indicated by the presence of fluorescently labeled MSC-Exos (PKH67 staining) within the F-actin cytoskeleton (phalloidin staining). MSC-Exos

resided within the cytosol and localized to the perinuclear region of the cytoplasm (adjacent to DAPI staining). Untreated AF cell controls showed no PKH67 staining indicating there was no uptake of MSC-Exos within the cytoplasm (**Fig. 5A**).

#### AF Cell Protection to Proinflammatory Cytokine Challenge

AF cells displayed an aberrant phenotype when challenged with 10 ng/mL  $\text{TNF}\alpha$  for 24 hours, indicated by a significant

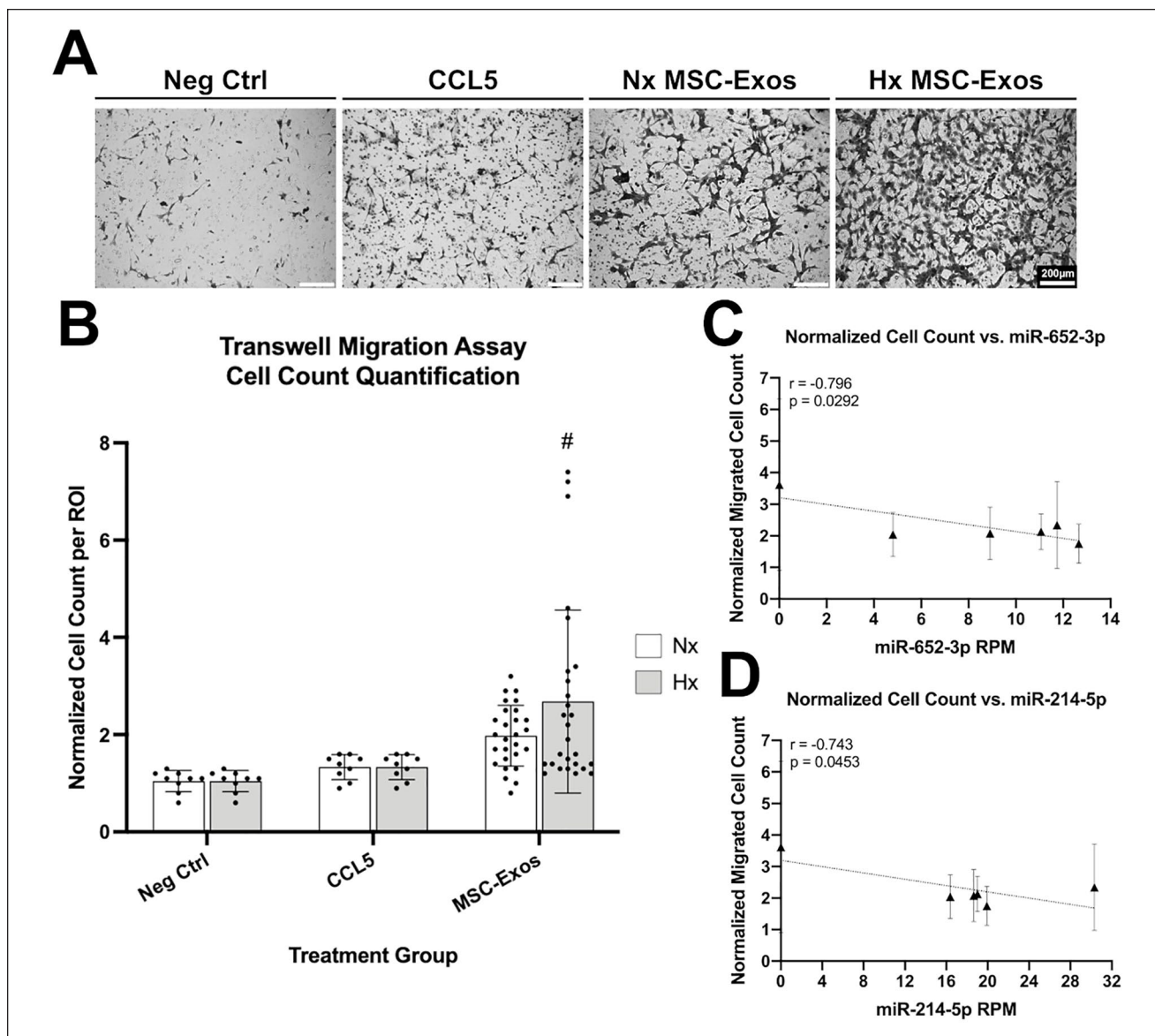


**Figure 4.** MSC-Exo treatment (50  $\mu\text{g}/\text{mL}$ ) elicits a chemotactic AF cell response after 24 hours. **(A)** AF cells stained with 0.2% (w/v) crystal violet on the underside of the transwell insert showed greatest migration for MSC-Exos. Objective = 10x; Scale bars = 200  $\mu\text{m}$ . **(B)** Quantification of migrated cells after 24 hours for 3 ROIs and 3 biological AF cell donors showed Hx MSC-Exos exhibited the significantly more migration.  $\#P < 0.05$  compared with negative control. Normalized migrated cell count correlated with **(C)** MSC-Exo miR-652-3p reads per million and **(D)** MSC-Exo miR-214-5p reads per million 24 hours after treatment at 50  $\mu\text{g}/\text{mL}$ . MSC-Exo = mesenchymal stem cell-derived exosome; AF = annulus fibrosus; ROIs = regions of interest.

decrease in *COL1A1*, *COL2A1*, *ACAN*, *SCX*, and *MKX* ( $P < 0.05$ ) and significant increase in *MMP1*, *IL6*, and *NLRP3* ( $P < 0.05$ ) compared with untreated controls. Hx MSC-Exo treatment at 50  $\mu\text{g}/\text{mL}$  for 24 hours was able to prevent some aberrant gene expression changes. In the MSC-Exo treatment group, AF cell gene expression was not statistically different from untreated controls for *COL1A1*, *ACAN*, *SCX*, *MKX*, and *MMP1* ( $P > 0.05$ ). However, treatment could not prevent the significant downregulation of *COL2A1* and the upregulation of *IL6* and *NLRP3* associated with  $\text{TNF}\alpha$  challenge (**Fig. 5B**).

### Morphology and PSD of PLGA $\mu\text{Spheres}$

PLGA  $\mu\text{Spheres}$  were fabricated using a sonication-free double emulsion method that successfully produced MSC-Exo carriers with spherical morphology for all vortexing conditions, as demonstrated by SEM imaging. Visual assessment of SEM images showed considerable polydispersity for all PLGA  $\mu\text{Sphere}$  fabrication groups. Laser diffraction analysis quantified the PSD for all PLGA  $\mu\text{Sphere}$  fabrication groups and statistically verified sample

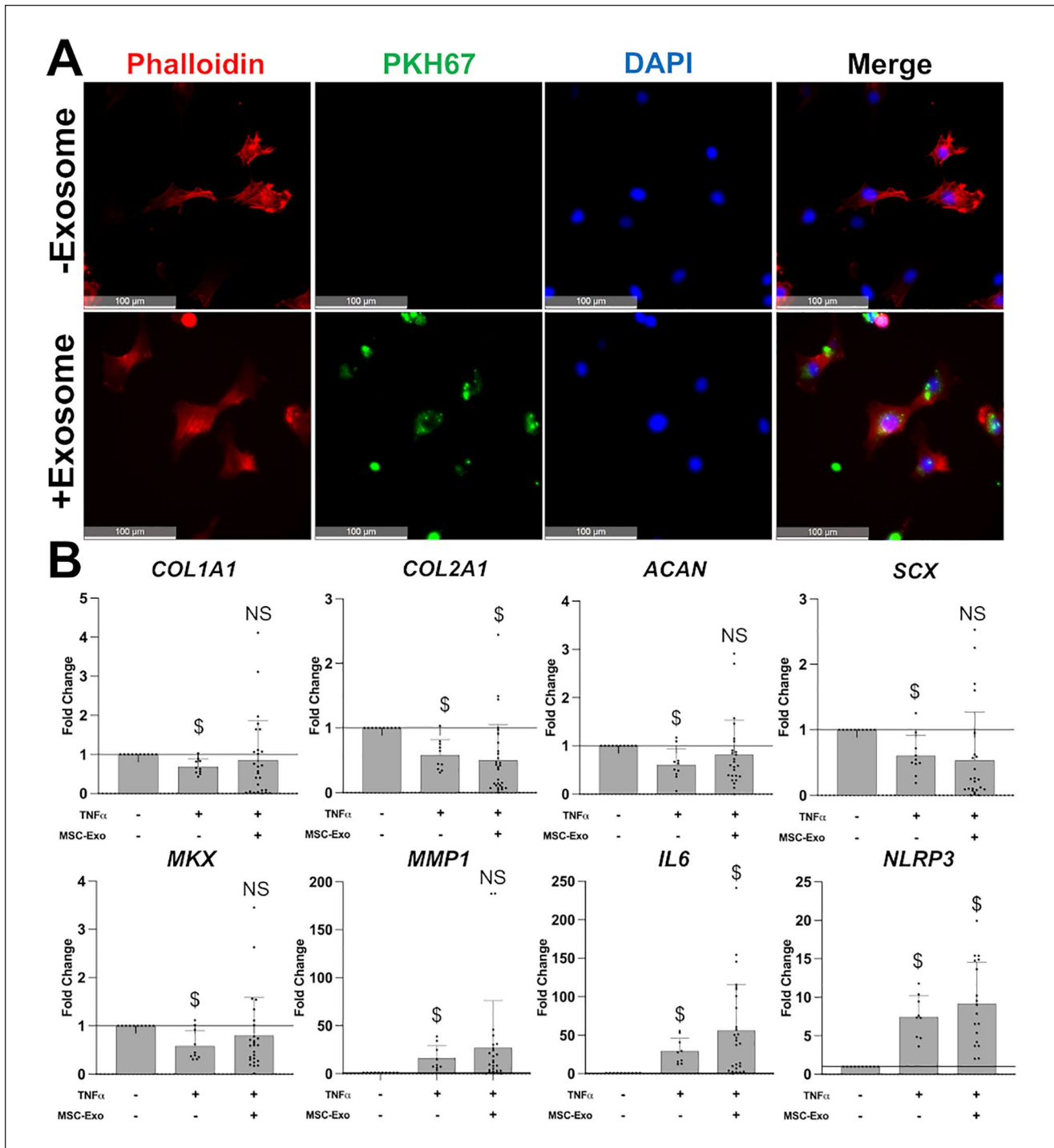


**Figure 5.** AF cells internalize MSC-Exos and maintain a healthy AF phenotype under a proinflammatory cytokine challenge with Hx MSC-Exo treatment at 50  $\mu\text{g}/\text{mL}$ . **(A)** Fluorescent labeling of MSC-Exos (PKH67), F-actin cytoskeleton (phalloidin), and cell nuclei (DAPI) demonstrates internalization within AF cells at 6 hours after MSC-Exo treatment. Objective = 40x; Scale bars = 100  $\mu\text{m}$ . **(B)** AF cell gene expression after 24 hours of TNF $\alpha$  (10 ng/mL)  $\pm$  Hx MSC-Exo (50  $\mu\text{g}/\text{mL}$ ) showed MSC-Exo treatment maintained control levels with TNF $\alpha$  challenge for multiple genes. AF = annulus fibrosus; MSC-Exo = mesenchymal stem cell-derived exosome; TNF $\alpha$  = tumor necrosis factor alpha; *COL1A1* = collagen type I alpha 1; *COL2A1* = collagen type II alpha 1; *ACAN* = aggrecan; *SCX* = scleraxis; *MKX* = Mohawk; *MMP1* = matrix metalloproteinase-1; *IL6* = interleukin 6; *NLRP3* = NLR family pyrin domain containing 3; NS = not significantly different than untreated controls. \$ $P < 0.05$  compared with untreated control.

polydispersity with a significant main effect across PSD percentiles ( $D_{10}$ , 10th percentile diameter;  $D_{50}$ , 50th percentile diameter; and  $D_{90}$ , 90th percentile diameter) ( $P < 0.0001$ ), but no significant effect of vortexing condition ( $P = 1.159$ ) or interaction ( $P = 0.893$ ) (**Fig. 6A**). SEM imaging showed that the sonication-free double emulsion method yields a heterogeneous internal structure of PLGA  $\mu$ Spheres, where some PLGA  $\mu$ Spheres were predominantly mononuclear whereas others were polynuclear with notable differences in nuclear size (**Fig. 6B**).

### Short-Term Effects of PLGA $\mu$ Sphere Integration within IPN Hydrogels

PLGA  $\mu$ Spheres were incorporated successfully within the IPN hydrogels and did not exhibit any degradation due to redox initiator exposure used for hydrogel cross-linking. SEM imaging indicated that the PLGA  $\mu$ Sphere carriers were homogeneously distributed within the hydrogel constructs, integrated within the bioadhesive polymer network (white arrows), and the corresponding visual density of PLGA  $\mu$ Spheres proportionally increased as the  $\mu$ Sphere concentration increased up to 5% (w/v) (**Fig. 6C**). Incorporated PLGA  $\mu$ Spheres within the IPN hydrogels did not result in a significant increase in the complex shear modulus ( $|G^*|$  ( $P > 0.05$ )); however, PLGA  $\mu$ Sphere incorporation did result in an increase in the tangent phase angle ( $\tan \delta$ ) at 2.5% (w/v) ( $P = 0.0007$ ) and 5% (w/v) ( $P = 0.0189$ )  $\mu$ Sphere concentrations (**Fig. 6D**).

### Long-Term Effects of PLGA $\mu$ Sphere Integration within IPN Hydrogels

Long-term culture of  $\mu$ Sphere-free and  $\mu$ Sphere-laden IPN hydrogels demonstrated a significant decrease in complex shear modulus ( $|G^*|(1 \text{ Hz})$ ) for all formulations as early as 7 days in culture compared with day 0 and monotonically decreased in magnitude through day 84 ( $p_{\text{time}} < 0.0001$ ). PLGA  $\mu$ Sphere concentration exhibited a significant effect on the complex shear modulus for long-term culture ( $p_{\text{concentration}} = 0.0082$ ) and significantly interacted with time over the 84-day period ( $p_{\text{interaction}} = 0.0003$ ). Conversely, the tangent phase angle ( $\tan \delta$ ) significantly increased for all formulations as early as 7 days in culture compared with day 0 and monotonically increased in magnitude through day 84 ( $p_{\text{time}} < 0.0001$ ), although values for  $\tan \delta$  remained very little indicating negligible dissipation. PLGA  $\mu$ Sphere concentration did not exhibit a significant effect on the tangent phase angle for long-term culture ( $p_{\text{concentration}} = 0.0603$ ), but significantly interacted with time over the 84-day period ( $p_{\text{interaction}} = 0.0169$ ) (**Fig. 7A**). Over the 84-day culture period, the pH of solution for all  $\mu$ Sphere-free and  $\mu$ Sphere-laden IPN hydrogel cultures remained within the pH range of 7.0 to 7.4. The only significant decreases in pH occurred

after the first 7 days of culture, and the pH remained significantly elevated from the original pH of solution at day 35 onward (**Fig. 7B**). IPN hydrogel wet weight steadily increased over time, where all formulations exhibited significantly higher wet weight by the end of the 84-day culture period compared with the initial wet weight (**Fig. 7C**). By day 84, the swelling ratio of all hydrogel formulations were not significantly different from one another (**Fig. 7D**), motivating an analysis of the hydrogel microstructure over the 84-day period.

SEM imaging demonstrated that the hydrogel microstructure was predominantly similar between the  $\mu$ Sphere-free and  $\mu$ Sphere-laden formulations, where the only observable difference between groups was the incorporation of PLGA  $\mu$ Spheres within the polymer network. Visual examination indicated that the hydrogel pore size increased over time and supports findings from wet weight and swelling ratio measurements (**Fig. 7E**). Quantitative analysis of SEM images indicated that there was a significant effect of time on hydrogel pore size ( $p_{\text{time}} < 0.0001$ ), where the pore size was significantly larger at day 84 compared with day 7 for all formulations ( $p_{0\%} < 0.0001$ ;  $p_{2.5\%} < 0.0001$ ;  $p_{5\%} < 0.0001$ ). Interestingly, there was a significant effect of  $\mu$ Sphere concentration ( $p_{\text{concentration}} < 0.0001$ ), as well as a significant interaction ( $p_{\text{interaction}} < 0.0001$ ), on pore size measurements (**Fig. 7F**). Examination of  $\mu$ Sphere-laden constructs at higher magnification showed a proportionally higher concentration of  $\mu$ Spheres in 5% (w/v) constructs compared with 2.5% (w/v) constructs at earlier timepoints, but differences in  $\mu$ Sphere density between formulations was considerably less discernable over time (**Fig. 7G**). Quantification of  $\mu$ Sphere count demonstrated a significant decrease over time ( $p_{\text{time}} = 0.0014$ ), with no significant effect of  $\mu$ Sphere concentration ( $p_{\text{concentration}} = 0.0603$ ) or interaction ( $p_{\text{interaction}} = 0.4323$ ) (**Fig. 7H**).

### Encapsulation of MSC-Exos in PLGA $\mu$ Spheres and Release Kinetics

Blank PLGA  $\mu$ Spheres exhibited a smooth surface topography and interior composition through SEM imaging (**Fig. 8A and B**). Histological analysis indicated an absence of OsO<sub>4</sub>-stained particles within the interior of the PLGA  $\mu$ Spheres, as well as the outer surface (**Fig. 8C**). MSC-Exo-laden  $\mu$ Spheres demonstrated particle speckling on the carrier surface and the inner PLGA core (white arrows) which was distinctly different from the smooth surface topography of the blank controls (**Fig. 8D and E**). Histological assessment of MSC-Exo-laden  $\mu$ Spheres also presented a distinctly different composition than the blank  $\mu$ Sphere controls, where the MSC-Exo-laden  $\mu$ Spheres featured OsO<sub>4</sub>-stained particles at the outer radius of the PLGA  $\mu$ Spheres, as well as the interior (black arrows) (**Fig. 8F**). Hydrogel-free MSC-Exo-laden  $\mu$ Spheres controlled

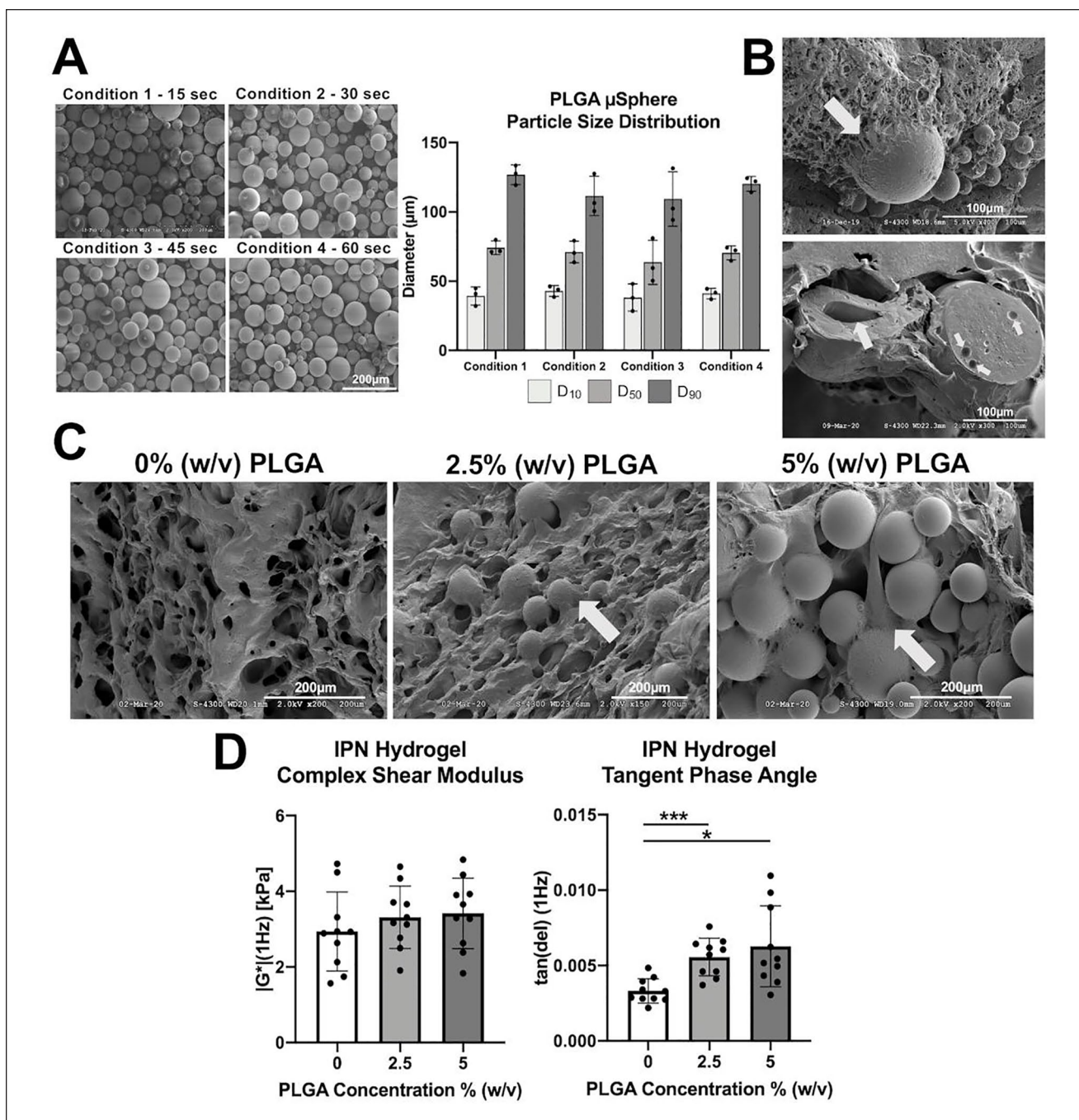


**Figure 6.** PLGA  $\mu$ Spheres integrate within the IPN hydrogel's bioadhesive polymer network, do not significantly increase the complex shear stiffness upon hydrogel embedment, and significantly increase the energy dissipation potential of the IPN hydrogel after equilibrium swelling. **(A)** SEM and laser diffraction analysis show no difference in  $\mu$ Sphere morphology or particle size distribution, respectively, when minimizing vortexing time in the double emulsion fabrication protocol.  $D_{10}$  = 10th percentile PLGA  $\mu$ Sphere diameter,  $D_{50}$  = 50th percentile PLGA  $\mu$ Sphere diameter, and  $D_{90}$  = 90th percentile PLGA  $\mu$ Sphere diameter. Panel A scale bar = 200  $\mu$ m. **(B)** SEM demonstrating hydrogel polymerization around the  $\mu$ Sphere surface upon embedment (white arrows—top image) and that  $\mu$ Spheres are mononuclear and polynuclear by composition (white arrows—bottom image). Panel B scale bar = 100  $\mu$ m. **(C)** Microstructure of the PLGA  $\mu$ Sphere delivery system within the IPN hydrogel for 2.5% (w/v) and 5% (w/v) conditions compared with  $\mu$ Sphere-free controls (0% [w/v]). Panel C scale bar = 200  $\mu$ m. **(D)** Complex shear stiffness ( $|G^*|$ ) and tangent phase angle ( $\tan \delta$ ) at 1 Hz for IPN hydrogels with 0% (w/v), 2.5% (w/v), and 5% (w/v) PLGA  $\mu$ Spheres after 72 hours of equilibrium swelling in 1X phosphate-buffered saline. PLGA = poly(lactic-co-glycolic acid); IPN = interpenetrating network; SEM = Scanning Electron Microscopy. \* $P < 0.05$ ; \*\*\* $P < 0.0005$ .

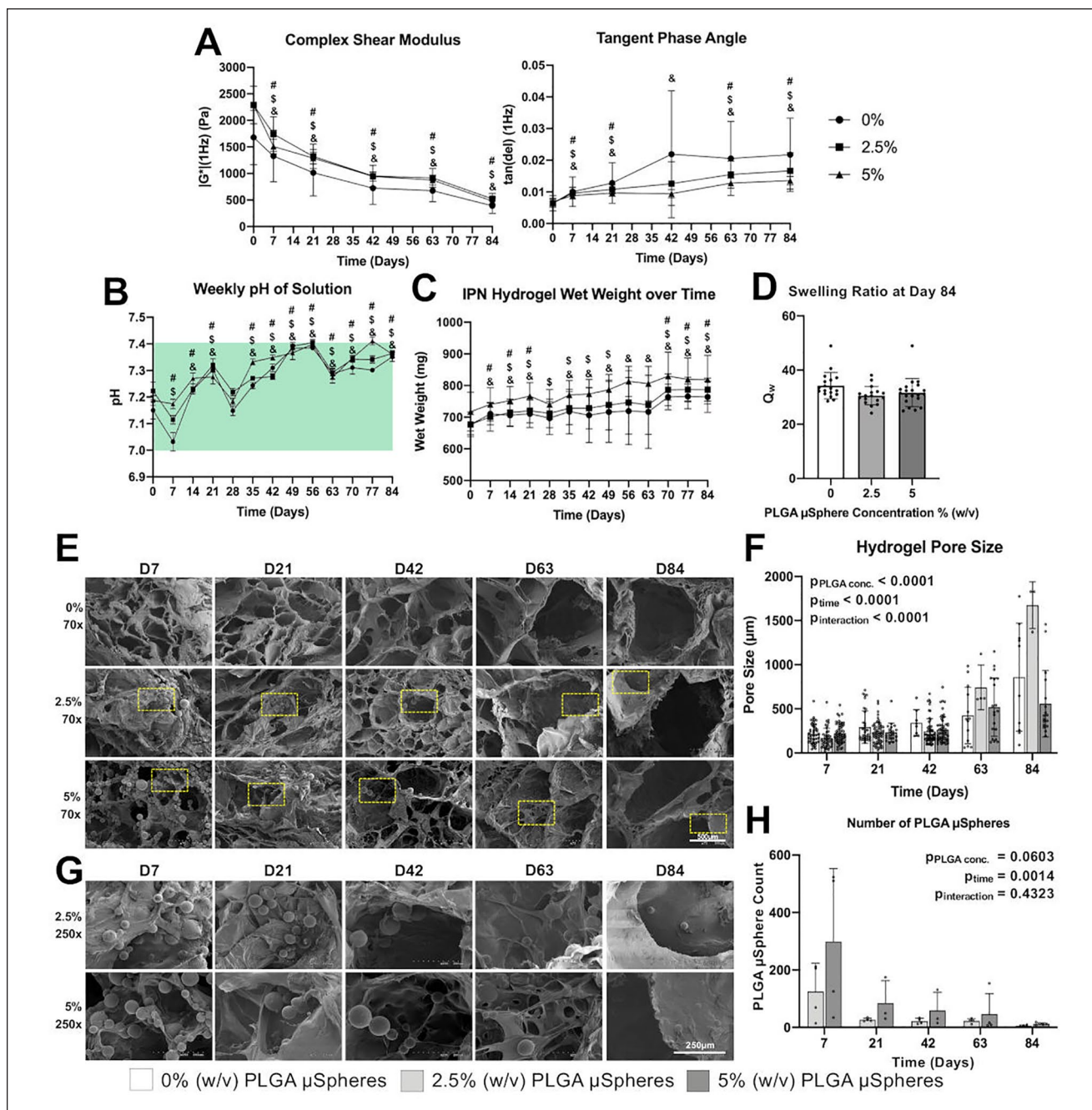


**Figure 7.** Long-term culture demonstrates that hydrogel-embedded PLGA  $\mu$ Spheres degrade over an 84-day period and leads to a significant decrease in biomechanical properties while maintaining a physiological pH range corresponding to that of a healthy IVD. (A) Complex shear stiffness ( $|G^*|$ ) and tangent phase angle ( $\tan \delta$ ) at 1Hz for IPN hydrogels with 0% (w/v), 2.5% (w/v), and 5% (w/v) PLGA  $\mu$ Spheres over an 84-day culture period. (B) Weekly pH of culture solution over the 84-day culture period for all hydrogel conditions. (C) IPN hydrogel wet weight over the 84-day culture period for all hydrogel conditions. (D) Swelling ratio ( $Q_w$ ) at day 84 for IPN hydrogels with 0% (w/v), 2.5% (w/v), and 5% (w/v) PLGA  $\mu$ Spheres. (E) SEM images of IPN hydrogel microstructure over the 84-day culture period for all hydrogel conditions. Yellow dashed box = regions corresponding to higher magnification SEM images in panel F. Objective = 70x; Scale bar = 500  $\mu$ m. (F) Quantification of hydrogel pore size after 7, 14, 21, 42, 63, and 84 days in culture. (G) SEM images of IPN hydrogel microstructure over the 84-day culture period for IPN hydrogels with 2.5% (w/v), and 5% (w/v) PLGA  $\mu$ Spheres. Objective = 250x; Scale bar = 250  $\mu$ m. (H) Quantification of PLGA  $\mu$ Sphere count embedded within the IPN hydrogels after 7, 14, 21, 42, 63, and 84 days in culture. PLGA = poly(lactic-co-glycolic acid); IVD = intervertebral disk; IPN = interpenetrating network; SEM = Scanning Electron Microscopy. #:  $P < 0.05$  at  $t_n$  compared with  $t_0$  for 0% (w/v) PLGA  $\mu$ Spheres; \$:  $P < 0.05$  at  $t_n$  compared with  $t_0$  for 2.5% (w/v) PLGA  $\mu$ Spheres; &:  $P < 0.05$  at  $t_n$  compared with  $t_0$  for 5% (w/v) PLGA  $\mu$ Spheres.

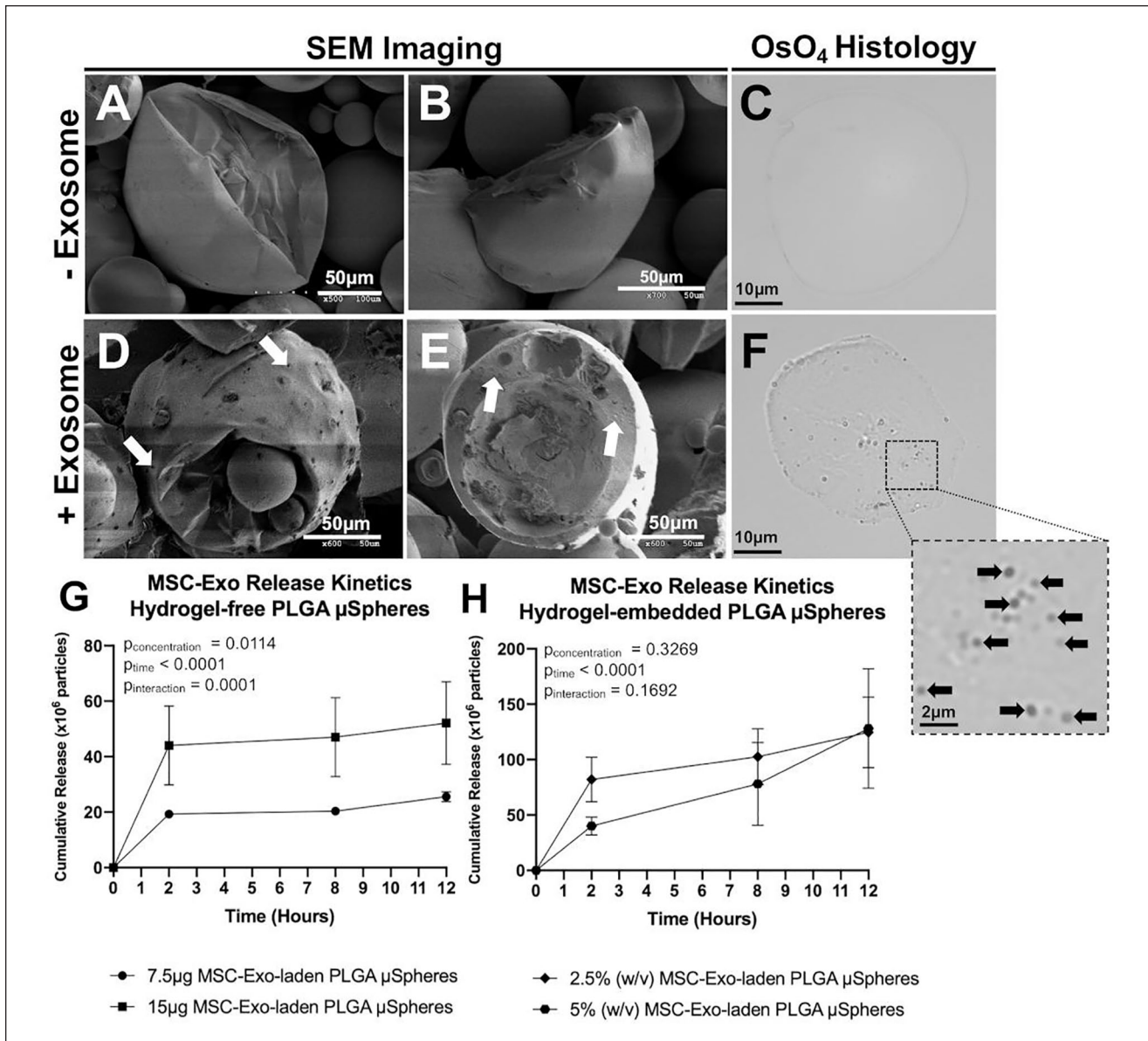


**Figure 8.** PLGA  $\mu$ Spheres demonstrate proof-of-concept MSC-Exo encapsulation and controlled release over a 12-hour period. **(A-B)** SEM of unloaded PLGA  $\mu$ Sphere controls. Scale bar = 50  $\mu$ m. **(C)** Histological assessment of OsO<sub>4</sub> stained blank PLGA  $\mu$ Sphere controls. Scale bar = 10  $\mu$ m. **(D-E)** SEM of MSC-Exo-loaded PLGA  $\mu$ Spheres. Scale bar = 50  $\mu$ m. **(F)** Histological assessment of OsO<sub>4</sub> stained MSC-Exo-loaded PLGA  $\mu$ Spheres. Scale bar = 10  $\mu$ m. Digitally zoomed scale bar = 2  $\mu$ m. **(G)** Release kinetics of MSC-Exo-loaded PLGA  $\mu$ Spheres not embedded in IPN hydrogels. **(H)** Release kinetics of MSC-Exo-loaded PLGA  $\mu$ Spheres embedded in IPN hydrogels. PLGA = poly(lactic-co-glycolic acid); MSC-Exo = mesenchymal stem cell-derived exosome; SEM = scanning electron microscopy; IPN = interpenetrating network.

the release of MSC-Exos from PLGA  $\mu$ Spheres over a 12-hour period, with significant effects of time and concentration as well as interaction (Fig. 8G). Hydrogel-embedded MSC-Exo-laden  $\mu$ Spheres demonstrated controlled release of MSC-Exos over a 12-hour period, with a significant effect of time, but no effect of concentration or interaction (Fig. 8H).

## Discussion

In this study, we investigate the potential of naive MSC-Exos as a new treatment strategy for biologically active AF repair without the need for exogenous stem cell transplantation, that are delivered in a biomaterial system capable of sustained release in an AF sealant. In the present work, we evaluate the ability of MSC-Exos to promote cellular



responses that would enhance the AF's innate endogenous repair capacity. Specifically, we determined that MSC-Exos promote proliferation, stimulate migration, and protect AF cells from aberrant phenotypes when exposed to a TNF $\alpha$  challenge. An MSC-Exo delivery system using PLGA  $\mu$ Spheres was developed and integrated within a bioadhesive hydrogel previously designed for AF repair.<sup>14</sup> We found that PLGA  $\mu$ Spheres can feasibly encapsulate and release MSC-Exos as well as integrate within the bioadhesive hydrogel network without affecting the hydrogel's mechanical properties or pH of the microenvironment as the  $\mu$ Spheres degrade. Taken together, these results point toward a new approach to simultaneously seal AF defects while delivering stem cell-derived vesicles that may enhance endogenous AF repair and decelerate the degenerative cascade.

Cell proliferation in response to MSC-Exo treatment is a key cellular response of interest, and our results indicate that MSC-Exos promote AF cell proliferation in a dose-dependent manner for all MSC-Exo treatment groups, where the greatest proliferative responses were observed at 72 hours following treatment. Therapeutic application of MSC-Exos to promote mitotic activity may prevent disease progression since cellular senescence is a pathological hallmark of IVDD.<sup>67</sup> pO<sub>2</sub> conditioning demonstrated differences in proliferative responses between Nx and Hx MSC-Exos. When relating AF cell proliferation to small RNA-Seq data, there was a significant and strong positive correlation between luminescent output and miR-21-5p, suggesting that this miR is involved in regulating cellular division. This finding corroborates with previous studies that empirically validated miR-21-5p to post-transcriptionally regulate PTEN, a known repressor of mitosis.<sup>40,68-71</sup> Overall, these outcomes demonstrate that naive MSC-Exos, particularly those containing high levels of miR-21-5p, can promote proliferation in an effort to repopulate the disk space with mitotically active cells and in turn mitigate the progression of IVDD.

Resident cell infiltration and stem cell homing are critical phenomena that support endogenous AF tissue repair, and our findings indicate that MSC-Exos, regardless of pO<sub>2</sub> conditioning environment, promoted AF cell migration when a chemotactic gradient was established with at least 50  $\mu$ g/mL.<sup>72-74</sup> Notably, Hx MSC-Exos produced the strongest migratory responses. When comparing AF cell migratory responses to the small RNA-seq data, hypoxic downregulation of miR-652-3p and miR-214-5p across all MSC-Exo donors may support our observation that Hx MSC-Exos induced a more robust migratory response than Nx MSC-Exos. These findings are in agreement with the significant and strong negative correlation between migrated cell count and miR-652-3p as well as miR-214-5p, suggesting that these miR transcripts regulate cell motility.

Downregulation of miR-652 may be implicated in increased AF cell migration by reduced targeting of poly(ADP-ribose) glycohydrolase (PARG) and vascular endothelial growth factor (VEGF) pathways.<sup>75</sup> Moreover, downregulation of miR-214 may result in increased AF cell migration by reduced targeting of PLAGL2.<sup>76</sup>

Since Hx preconditioned MSC-Exos demonstrated the most robust cellular responses with respect to AF cell proliferation and migration, we selected this MSC-Exo pO<sub>2</sub> group for downstream use to treat TNF $\alpha$ -challenged AF cells. This *in vitro* system is useful to simulate the proinflammatory microenvironment analogous to that of IVDD and determine whether MSC-Exos can protect AF cells from an aberrant phenotype that emulates one found in IVDD pathologies.<sup>77</sup> Following treatment, AF cells internalized MSC-Exos within 6 hours and were localized in the perinuclear and cytosolic spaces, suggesting that these particles can modulate AF cell expression through post-transcriptional repression and mRNA destabilization once their small RNA cargo is released intracellularly.<sup>78-80</sup> Our study supports the concept that naive MSC-Exos exert a protective effect against TNF $\alpha$ -induced damage as indicated by their gene expression levels that were comparable to the untreated control for many genes that are associated with a normal AF phenotype (i.e., *COL1A1*, *ACAN*, *SCX*, and *MKX*).<sup>81</sup> Moreover, we found that MSC-Exos can modulate catabolic and inflammatory responses in AF cells by attenuating *MMP1* expression, which is implicated in IVDD pathogenesis.<sup>82,83</sup> Outcomes in our study corroborate with complementary findings in the only prior study that examines MSC-Exo treatment on AF cells.<sup>84</sup> Notably, AF cells were challenged with IL1 $\beta$  instead of TNF $\alpha$  in the previous study, which is also associated with IVDD-related inflammation.<sup>85</sup> However, IL1 $\beta$  elicits distinctly different responses in AF cell gene expression than TNF $\alpha$  due to differences in respective intracellular signaling cascades, motivating the present study to determine the protective effects of MSC-Exos on AF cells when challenged with TNF $\alpha$ .<sup>86-88</sup> Nevertheless, the present study and previous work substantiate the therapeutic potential of MSC-Exos for AF repair in the context of proinflammatory conditions.

To achieve clinical utility of an MSC-Exo treatment strategy, an integrated drug delivery system is required to enable sustained release of biological cargo and to seal IVD defects to prevent leakage. PLGA  $\mu$ Spheres are widely used to deliver biologics, and their use to deliver exosomes is just starting to emerge in regenerative medicine.<sup>65,66</sup> A bioadhesive IPN hydrogel is also used to seal AF defects and retain PLGA  $\mu$ Spheres within the repair site.<sup>14</sup> Given the central role of mechanics in IVD physiology, AF-specific applications must determine whether drug delivery systems impart biomechanical changes in AF repair hydrogels. The present work therefore evaluated the short-term and long-term effects of PLGA  $\mu$ Sphere integration on mechanical and

biomaterial properties. In our previous study, we found that the herniation risk was inversely proportional to the hydrogel modulus.<sup>14</sup> Since IVD herniation risk is a clinical design priority for AF repair hydrogels, a design requirement posed for the current study was to not affect the modulus of the IPN hydrogel system when fabricating hydrogel composites with PLGA  $\mu$ Spheres.<sup>89-93</sup> Although there were visual differences in network structure, the complex shear modulus was not significantly different between composite and  $\mu$ Sphere-free hydrogels, suggesting that the herniation risk is unchanged when repairing AF defects with PLGA  $\mu$ Sphere-IPN hydrogel composites.

Controlled release of MSC-Exos and associated tissue repair responses are contingent on long-term degradation of the IPN hydrogel system and PLGA  $\mu$ Spheres, warranting the characterization of time-dependent properties for this treatment strategy in long-term culture.<sup>94,95</sup> The SEM findings demonstrate that the polymer network is visually less dense with a significant increase in pore size over time, indicating that hydrogel degradation occurs substantially within a 84-day period. Degradation-related changes in polymer network architecture corroborate with temporal changes in mechanical properties, where the complex shear modulus monotonically decreases over time, while the tangent phase angle monotonically increases over time.<sup>96,97</sup> Given that AF cells are under 20  $\mu$ m in diameter, pore size measurements suggest that this hydrogel system would easily permit cellular infiltration.<sup>98</sup> To promote AF cell infiltration, PLGA  $\mu$ Spheres must simultaneously degrade so as to release the MSC-Exo payload into the surrounding environment and establish a chemotactic gradient. When quantifying the hydrogel-embedded PLGA  $\mu$ Spheres in long-term culture, we found that  $\mu$ Spheres significantly degrade over an 84-day period and may sustain continuous MSC-Exo release. The limited transport of the avascular IVD has highlighted pH as an important factor in IVD repair strategies, so it was necessary to examine culture pH during PLGA  $\mu$ Sphere degradation.<sup>20,53,99</sup> By composition, PLGA is a copolymer of 2 acidic monomers that hydrolytically degrades into these 2 byproducts over time. Our findings indicate that incorporating up to 5% (w/v) PLGA  $\mu$ Spheres in IPN hydrogels enabled maintenance of a stable physiologically healthy pH range over the 84-day period, suggesting PLGA degradation would not deleteriously affect the IVD pH during repair.<sup>100</sup>

Drug delivery systems enable controlled biologic release, prevent rapid clearance, and allow for single dose administration, which leads to enhanced regenerative outcomes compared with bioinert strategies without integrated delivery systems.<sup>101</sup> Here, we utilize a sonication-free double emulsion fabrication protocol to generate PLGA  $\mu$ Spheres with an MSC-Exo payload, while minimizing vortex perturbation time during fabrication. Exosomes are more sensitive to  $\mu$ Sphere fabrication conditions than other biologics traditionally

delivered with PLGA  $\mu$ Spheres, and our histological findings support the use of this adapted sonication-free technique to generate MSC-Exo-loaded PLGA  $\mu$ Spheres. SEM and histological findings indicate successful MSC-Exo encapsulation within PLGA  $\mu$ Spheres and NTA quantification exhibits sustained release of MSC-Exos from the carrier with and without the hydrogel, demonstrating technical feasibility of this drug delivery system for bioactive AF repair in IVDD conditions with and without large defects. Together, these outcomes suggest this delivery system would achieve these 2 primary objectives since  $\mu$ Spheres embed in the bioadhesive hydrogel during polymerization and would consequentially remain within the AF repair site.

There are a few limitations associated with the present study and key avenues of future directions that would advance this novel treatment strategy toward clinical application. Although this study directly measures MSC-Exo release kinetics from PLGA  $\mu$ Spheres *via* NTA, it is not known whether the MSC-Exo concentration in the releasate elicits the most robust therapeutic responses in AF cells, and our duration is limited to 12 hours. Two prior studies in craniofacial tissue engineering utilized an analogous approach to deliver MSC-Exos from PLGA  $\mu$ Spheres in dental pulp tissue and found that MSC-Exos maintain their bioactivity throughout encapsulation and release processes.<sup>65,66</sup> While it is a limitation that long-term kinetics and the degree of AF cell responses are not known, we anticipate that the MSC-Exos will continue to be released and retain their bioactivity as the particle concentration is a corollary for the RNA released into the culture environment. Future work will optimize PLGA  $\mu$ Sphere formulations with respect to polymer molecular weight and lactic acid to glycolic acid ratios in order to optimize MSC-Exo release kinetics and achieve MSC-Exo releasate concentrations that maximize therapeutic responses. Another limitation is the *in vitro* focus of this study, where this study focused on functional evaluation of AF cell responses to MSC-Exo treatment and biomaterial delivery system development and characterization. Preclinical models of IVDD *in vivo* are important next steps to study this AF treatment strategy in the context of interconnected systems with the IVD, including neurological pain behaviors and immune system responses.

## Conclusions

This study is the first to develop a combination strategy composed of a bioadhesive PLGA  $\mu$ Sphere-IPN hydrogel composite system to deliver MSC-Exos for bioactive AF repair. MSC-Exos offer distinct advantages over cell delivery strategies in IVD regenerative medicine to confer the therapeutic benefits of stem cells, while circumventing translational obstacles in IVD cell therapy. Here, we show that MSC-Exos can (1) promote proliferative and chemotactic AF cell responses,

(2) modulate AF cell expression through post-transcriptional regulation and protect against aberrant phenotypes associated with IVDD, and (3) be encapsulated within PLGA  $\mu$ Spheres for controlled release in IVDD conditions with and without AF defects. Our results provide strong evidence to suggest that MSC-Exos are a promising therapeutic for IVDD and may enhance the AF's poor intrinsic repair capacity by directing pro-regenerative responses in resident AF cells without the need for exogenous stem cell transplantation.

### Author Contributions

Conceptualization, T.J.D.; Study Design Discussion, T.J.D., S.S., J.R.W., and J.C.I.; Primary Experimentation/Data Acquisition, T.J.D., K.V., G.D., H.N.C., K.K., and S.Z.K.; Data Post-processing, T.J.D., K.V., M.W., and P.X.; Writing – Original Draft, T.J.D.; Writing – Review & Editing, T.J.D., K.V., C.J.P., G.D., H.N.C., K.K., S.Z.K., M.W., P.X., R.N.D., S.S., J.R.W., and J.C.I.; Supervision & Project Administration, T.J.D. and J.C.I.; Funding Acquisition, T.J.D. and J.C.I.

### Acknowledgments and Funding

This work was supported by NIH/NIAMS Grants R01 AR057397 & R01AR080096, and NIH/NIGMS Grant T32 GM062754. Confocal microscopy was performed at the Microscopy CoRE at the Icahn School of Medicine at Mount Sinai. We thank trainees in Dr. Susmita Sahoo's laboratory in the Cardiovascular Research Center for technical training on MSC-Exo isolation protocols and access to facilities. We gratefully acknowledge Andrew Paul Leonard and Dr. Ronald Gordon at the Mount Sinai Pathology Core Facility for access and technical assistance with SEM and TEM imaging. Also, we gratefully acknowledge Dr. Rachel Derita at the Penn Vet Extracellular Vesicle Core for technical assistance running MSC-Exo releasate samples on the ZetaView NTA instrument. Lastly, we thank Dr. Andrew C. Hecht for his clinical expertise and input.

### Declaration of Conflicting Interests

The author(s) declared no potential conflicts of interest with respect to the research, authorship, and/or publication of this article.

### Ethical Approval

Ethical approval was not sought for the present study because post-mortem bovine tissue and mesenchymal stem cells utilized in this study were purchased from third party vendors.

### ORCID iDs

Tyler J. DiStefano  <https://orcid.org/0000-0001-9406-3085>

James C. Iatridis  <https://orcid.org/0000-0002-2186-0590>

### References

- Hartvigsen J, Hancock MJ, Kongsted A, Louw Q, Ferreira ML, Genevay S, *et al.* What low back pain is and why we need to pay attention. *Lancet*. 2018;391:2356-67. doi:10.1016/S0140-6736(18)30480-X.
- Michalek AJ, Iatridis JC. Height and torsional stiffness are most sensitive to annular injury in large animal intervertebral discs. *Spine J*. 2012;12:425-32. doi:10.1016/j.spinee.2012.04.001.
- Long RG, Ferguson SJ, Benneker LM, Sakai D, Li Z, Pandit A, *et al.* Morphological and biomechanical effects of annulus fibrosus injury and repair in an ovine cervical model. *JOR Spine*. 2020;3:e1074. doi:10.1002/jsp2.1074.
- Sharma A, Pilgram T, Wippold FJ II. Association between annular tears and disk degeneration: a longitudinal study. *AJNR Am J Neuroradiol*. 2009;30:500-6. doi:10.3174/ajnr.A1411.
- Osti OL, Vernon-Roberts B, Fraser RD. 1990 Volvo Award in experimental studies. Annulus tears and intervertebral disc degeneration. An experimental study using an animal model. *Spine*. 1990;15:762-7.
- Hampton D, Laros G, McCarron R, Franks D. Healing potential of the annulus fibrosus. *Spine*. 1989;14:398-401. doi:10.1097/00007632-198904000-00009.
- Smith JW, Walmsley R. Experimental incision of the intervertebral disc. *J Bone Joint Surg Br*. 1951;33-B:612-25. doi:10.1302/0301-620X.33B4.612.
- Grunert P, Borde BH, Towne SB, Moriguchi Y, Hudson KD, Bonassar LJ, *et al.* Riboflavin crosslinked high-density collagen gel for the repair of annular defects in intervertebral discs: an in vivo study. *Acta Biomater*. 2015;26:215-24. doi:10.1016/j.actbio.2015.06.006.
- Carragee EJ, Han MY, Suen PW, Kim D. Clinical outcomes after lumbar discectomy for sciatica: the effects of fragment type and annular competence. *J Bone Joint Surg Am*. 2003;85:102-8.
- Carragee EJ, Spinnickie AO, Alamin TF, Paragioudakis S. A prospective controlled study of limited versus subtotal posterior discectomy: short-term outcomes in patients with herniated lumbar intervertebral discs and large posterior annular defect. *Spine*. 2006;31:653-7. doi:10.1097/01.brs.0000203714.76250.68.
- Miller LE, McGirt MJ, Garfin SR, Bono CM. Association of annular defect width after lumbar discectomy with risk of symptom recurrence and reoperation: systematic review and meta-analysis of comparative studies. *Spine*. 2018;43:E308-15. doi:10.1097/BRS.0000000000002501.
- Ammerman J, Watters WC, Inzana JA, Carragee G, Groff MW. Closing the treatment gap for lumbar disc herniation patients with large annular defects: a systematic review of techniques and outcomes in this high-risk population. *Cureus*. 2019;11:e4613. doi:10.7759/cureus.4613.
- Guterl CC, See EY, Blanquer SBG, Pandit A, Ferguson SJ, Benneker LM, *et al.* Challenges and strategies in the repair of ruptured annulus fibrosus. *Eur Cell Mater*. 2013;25:1-21. doi:10.22203/eCM.v025a01.
- DiStefano TJ, Shmukler JO, Daniais G, Di Pauli von Treuheim T, Hom WW, Goldberg DA, *et al.* Development of a two-part biomaterial adhesive strategy for annulus fibrosus repair and ex vivo evaluation of implant herniation risk. *Biomaterials*. 2020;258:120309. doi:10.1016/j.biomaterials.2020.120309.
- Vadalà G, Sowa G, Hubert M, Gilbertson LG, Denaro V, Kang JD. Mesenchymal stem cells injection in degenerated

- intervertebral disc: cell leakage may induce osteophyte formation. *J Tissue Eng Regen Med.* 2012;6:348-55. doi:10.1002/term.433.
16. Varden LJ, Nguyen DT, Michalek AJ. Slow depressurization following intradiscal injection leads to injectate leakage in a large animal model. *JOR Spine.* 2019;2:e1061. doi:10.1002/jsp2.1061.
  17. Bertram H, Kroeber M, Wang H, Unglaub F, Guehring T, Carstens C, *et al.* Matrix-assisted cell transfer for intervertebral disc cell therapy. *Biochem Biophys Res Commun.* 2005;331:1185-92. doi:10.1016/j.bbrc.2005.04.034.
  18. Li YY, Diao HJ, Chik TK, Chow CT, An XM, Leung V, *et al.* Delivering mesenchymal stem cells in collagen microsphere carriers to rabbit degenerative disc: reduced risk of osteophyte formation. *Tissue Eng Part A.* 2014;20:1379-91. doi:10.1089/ten.TEA.2013.0498.
  19. Smith LJ, Silverman L, Sakai D, Le Maitre CL, Mauck RL, Malhotra NR, *et al.* Advancing cell therapies for intervertebral disc regeneration from the lab to the clinic: recommendations of the ORS spine section. *JOR Spine.* 2018;1:e1036. doi:10.1002/jsp2.1036.
  20. Huang YC, Urban JP, Luk KD. Intervertebral disc regeneration: do nutrients lead the way? *Nat Rev Rheumatol.* 2014;10:561-6. doi:10.1038/nrrheum.2014.91.
  21. Kandel R, Roberts S, Urban JPG. Tissue engineering and the intervertebral disc: the challenges. *Eur Spine J.* 2008;17(Suppl 4):480-91. doi:10.1007/s00586-008-0746-2.
  22. Panebianco CJ, Meyers JH, Gansau J, Hom WW, Iatridis JC. Balancing biological and biomechanical performance in intervertebral disc repair: a systematic review of injectable cell delivery biomaterials. *eCM.* 2020;40:239-58. doi:10.22203/eCM.v040a15.
  23. Wuertz K, Godburn K, Neidlinger-Wilke C, Urban J, Iatridis JC. Behavior of mesenchymal stem cells in the chemical microenvironment of the intervertebral disc. *Spine.* 2008;33:1843-9. doi:10.1097/BRS.0b013e31817b8f53.
  24. Wuertz K, Godburn K, Iatridis JC. MSC response to pH levels found in degenerating intervertebral discs. *Biochem Biophys Res Commun.* 2009;379:824-9. doi:10.1016/j.bbrc.2008.12.145.
  25. Naqvi SM, Buckley CT. Extracellular matrix production by nucleus pulposus and bone marrow stem cells in response to altered oxygen and glucose microenvironments. *J Anat.* 2015;227:757-66. doi:10.1111/joa.12305.
  26. Naqvi SM, Buckley CT. Bone marrow stem cells in response to intervertebral disc-like matrix acidity and oxygen concentration: implications for cell-based regenerative therapy. *Spine.* 2016;41:743-50. doi:10.1097/BRS.0000000000001314.
  27. Loibl M, Wuertz-Kozak K, Vadala G, Lang S, Fairbank J, Urban JP. Controversies in regenerative medicine: should intervertebral disc degeneration be treated with mesenchymal stem cells. *JOR Spine.* 2019;2:e1043. doi:10.1002/jsp2.1043.
  28. Li JJ, Hosseini-Beheshti E, Grau GE, Zreiqat H, Little CB. Stem cell-derived extracellular vesicles for treating joint injury and osteoarthritis. *Nanomaterials (Basel).* 2019;9:261. doi:10.3390/nano9020261.
  29. Mianehsaz E, Mirzaei HR, Mahjoubin-Tehran M, Rezaee A, Sahebnaasagh R, Pourhanifeh MH, *et al.* Mesenchymal stem cell-derived exosomes: a new therapeutic approach to osteoarthritis? *Stem Cell Res Ther.* 2019;10:340. doi:10.1186/s13287-019-1445-0.
  30. Malda J, Boere J, van de Lest CH, van Weeren P, Wauben MH. Extracellular vesicles new tool for joint repair and regeneration. *Nat Rev Rheumatol.* 2016;12:243-9. doi:10.1038/nrrheum.2015.170.
  31. Boere J, Malda J, van de Lest CHA, van Weeren PR, Wauben MHM. Extracellular vesicles in joint disease and therapy. *Front Immunol.* 2018;9:2575. doi:10.3389/fimmu.2018.02575.
  32. Phinney DG, Pittenger MF. Concise review: MSC-derived exosomes for cell-free therapy. *Stem Cells.* 2017;35:851-8. doi:10.1002/stem.2575.
  33. Yin K, Wang S, Zhao RC. Exosomes from mesenchymal stem/stromal cells: a new therapeutic paradigm. *Biomark Res.* 2019;7:8. doi:10.1186/s40364-019-0159-x.
  34. Xia C, Zeng Z, Fang B, Tao M, Gu C, Zheng L, *et al.* Mesenchymal stem cell-derived exosomes ameliorate intervertebral disc degeneration via anti-oxidant and anti-inflammatory effects. *Free Radic Biol Med.* 2019;143:1-15. doi:10.1016/j.freeradbiomed.2019.07.026.
  35. Lu K, Li H-Y, Yang K, Wu J-L, Cai X-W, Zhou Y, *et al.* Exosomes as potential alternatives to stem cell therapy for intervertebral disc degeneration: in-vitro study on exosomes in interaction of nucleus pulposus cells and bone marrow mesenchymal stem cells. *Stem Cell Res Ther.* 2017;8:108. doi:10.1186/s13287-017-0563-9.
  36. Bach FC, de Vries SA, Riemers FM, Boere J, van Heel FW, van Doeselaar M, *et al.* Soluble and pelletable factors in porcine, canine and human notochordal cell-conditioned medium: implications for IVD regeneration. *Eur Cell Mater.* 2016;32:163-80. doi:10.22203/eCM.v032a11.
  37. Bach F, Libregts S, Creemers L, Meij B, Ito K, Wauben M, *et al.* Notochordal-cell derived extracellular vesicles exert regenerative effects on canine and human nucleus pulposus cells. *Oncotarget.* 2017;8:88845-56. doi:10.18632/oncotarget.21483.
  38. Lan WR, Pan S, Li H-Y, Sun C, Chang X, Lu K, *et al.* Inhibition of the Notch1 pathway promotes the effects of nucleus pulposus cell-derived exosomes on the differentiation of mesenchymal stem cells into nucleus pulposus-like cells in rats. *Stem Cells Int.* 2019;2019:8404168. doi:10.1155/2019/8404168.
  39. Qi L, Wang R, Shi Q, Yuan M, Jin M, Li D. Umbilical cord mesenchymal stem cell conditioned medium restored the expression of collagen II and aggrecan in nucleus pulposus mesenchymal stem cells exposed to high glucose. *J Bone Miner Metab.* 2019;37:455-66. doi:10.1007/s00774-018-0953-9.
  40. Cheng X, Zhang G, Zhang L, Hu Y, Zhang K, Sun X, *et al.* Mesenchymal stem cells deliver exogenous miR-21 via exosomes to inhibit nucleus pulposus cell apoptosis and reduce intervertebral disc degeneration. *J Cell Mol Med.* 2018;22:261-76. doi:10.1111/jcmm.13316.
  41. Bari E, Perteghella S, Di Silvestre D, Sorlini M, Catenacci L, Sorrenti M, *et al.* Pilot production of mesenchymal stem/stromal freeze-dried secretome for cell-free regenerative nanomedicine: a validated GMP-compliant process. *Cells.* 2018;7:190. doi:10.3390/cells7110190.

42. Liao Z, Luo R, Li G, Song Y, Zhan S, Zhao K, *et al.* Exosomes from mesenchymal stem cells modulate endoplasmic reticulum stress to protect against nucleus pulposus cell death and ameliorate intervertebral disc degeneration in vivo. *Theranostics*. 2019;9:4084-100. doi:10.7150/thno.33638.
43. DiStefano TJ, Vaso K, Danias G, Chionuma HN, Weiser JR, Iatridis JC. Extracellular vesicles as an emerging treatment option for intervertebral disc degeneration: therapeutic potential, translational pathways, and regulatory considerations. *Adv Healthc Mater*. 2022;11:e2100596. doi:10.1002/adhm.202100596.
44. Pattappa G, Li Z, Peroglio M, Wismer N, Alini M, Grad S. Diversity of intervertebral disc cells: phenotype and function. *J Anat*. 2012;221:480-96. doi:10.1111/j.1469-7580.2012.01521.x.
45. van den Akker GG, Vitters EL, Davidson ENB, van der Kraan PM. Intervertebral disc homeostasis: site-specific activity of transforming growth factor in the nucleus pulposus and annulus fibrosus. *Osteoarthr Cartil*. 2017;25:S402-3. doi:10.1016/j.joca.2017.02.693.
46. Torre OM, Mroz V, Bartelstein MK, Huang AH, Iatridis JC. Annulus fibrosus cell phenotypes in homeostasis and injury: implications for regenerative strategies. *Ann N Y Acad Sci*. 2019;1442:61-78. doi:10.1111/nyas.13964.
47. Ludwig N, Whiteside TL, Reichert TE. Challenges in exosome isolation and analysis in health and disease. *Int J Mol Sci*. 2019;20:4684. doi:10.3390/ijms20194684.
48. Kucharzewska P, Christianson HC, Welch JE, Svensson KJ, Fredlund E, Ringnér M, *et al.* Exosomes reflect the hypoxic status of glioma cells and mediate hypoxia-dependent activation of vascular cells during tumor development. *Proc Natl Acad Sci USA*. 2013;110:7312-7. doi:10.1073/pnas.1220998110.
49. Truong G, Guanzon D, Kinhal V, Elfeky O, Lai A, Longo S, *et al.* Oxygen tension regulates the miRNA profile and bioactivity of exosomes released from extravillous trophoblast cells—liquid biopsies for monitoring complications of pregnancy. *PLoS ONE*. 2017;12:e0174514. doi:10.1371/journal.pone.0174514.
50. Namazi H, Mohit E, Namazi I, Rajabi S, Samadian A, Hajizadeh-Saffar E, *et al.* Exosomes secreted by hypoxic cardiosphere-derived cells enhance tube formation and increase pro-angiogenic miRNA. *J Cell Biochem*. 2018;119:4150-60. doi:10.1002/jcb.26621.
51. Danhier F, Ansorena E, Silva JM, Coco R, Le Breton A, Prétat V. PLGA-based nanoparticles: an overview of biomedical applications. *J Control Release*. 2012;161:505-22. doi:10.1016/j.jconrel.2012.01.043.
52. Elmowafy EM, Tiboni M, Soliman ME. Biocompatibility, biodegradation and biomedical applications of poly(lactic acid)/poly(lactic-co-glycolic acid) micro and nanoparticles. *J Pharm Investig*. 2019;49:347-80. doi:10.1007/s40005-019-00439-x.
53. Gilbert HTJ, Hodson N, Baird P, Richardson SM, Hoyland JA. Acidic pH promotes intervertebral disc degeneration: acid-sensing ion channel -3 as a potential therapeutic target. *Sci Rep*. 2016;6:37360. doi:10.1038/srep37360.
54. Bibby SRS, Jones DA, Ripley RM, Urban JPG. Metabolism of the intervertebral disc: effects of low levels of oxygen, glucose, and pH on rates of energy metabolism of bovine nucleus pulposus cells. *Spine*. 2005;30:487-96. doi:10.1097/01.brs.0000154619.38122.47.
55. Peck SH, Bendigo JR, Tobias JW, Dodge GR, Malhotra NR, Mauck RL, *et al.* Hypoxic preconditioning enhances bone marrow-derived mesenchymal stem cell survival in a low oxygen and nutrient-limited 3D microenvironment. *Cartilage*. 2021;12:512-25. doi:10.1177/1947603519841675.
56. Sahoo S, Klychko E, Thorne T, Misener S, Schultz KM, Millay M, *et al.* Exosomes from human CD34(+) stem cells mediate their proangiogenic paracrine activity. *Circ Res*. 2011;109:724-8. doi:10.1161/CIRCRESAHA.111.253286.
57. Théry C, Amigorena S, Raposo G, Clayton A. Isolation and characterization of exosomes from cell culture supernatants and biological fluids. *Curr Protoc Cell Biol*. 2006; Chapter 3:Unit 3.22. doi:10.1002/0471143030.cb0322s30.
58. Liu J, Zhu S, Tang W, Huang Q, Mei Y, Yang H. Exosomes from tamoxifen-resistant breast cancer cells transmit drug resistance partly by delivering miR-9-5p. *Cancer Cell Int*. 2021;21:55. doi:10.1186/s12935-020-01659-0.
59. Zhao L, Yu J, Wang J, Li H, Che J, Cao B. Isolation and Identification of miRNAs in exosomes derived from serum of colon cancer patients. *J Cancer*. 2017;8:1145-52. doi:10.7150/jca.18026.
60. Robinson MD, Oshlack A. A scaling normalization method for differential expression analysis of RNA-seq data. *Genome Biol*. 2010;11:R25. doi:10.1186/gb-2010-11-3-r25.
61. Ritchie ME, Phipson B, Wu D, Hu Y, Law CW, Shi W, *et al.* limma powers differential expression analyses for RNA-sequencing and microarray studies. *Nucleic Acids Res*. 2015;43:e47. doi:10.1093/nar/gkv007.
62. Justus CR, Leffler N, Ruiz-Echevarria M, Yang LV. In vitro cell migration and invasion assays. *J Vis Exp*. 2014;88:51046. doi:10.37971/51046.
63. Tarafder S, Koch A, Jun Y, Chou C, Awadallah MR, Lee CH. Micro-precise spatiotemporal delivery system embedded in 3D printing for complex tissue regeneration. *Biofabrication*. 2016;8:025003. doi:10.1088/1758-5090/8/2/025003.
64. Costi JJ, Stokes IA, Gardner-Morse MG, Iatridis JC. Frequency-dependent behavior of the intervertebral disc in response to each of six degree of freedom dynamic loading: solid phase and fluid phase contributions. *Spine*. 2008;33:1731-8. doi:10.1097/BRS.0b013e31817bb116.
65. Swanson WB, Gong T, Zhang Z, Eberle M, Niemann D, Dong R, *et al.* Controlled release of odontogenic exosomes from a biodegradable vehicle mediates dentinogenesis as a novel biomimetic pulp capping therapy. *J Control Release*. 2020;324:679-94. doi:10.1016/j.jconrel.2020.06.006.
66. Swanson WB, Zhang Z, Xiu K, Gong T, Eberle M, Wang Z, *et al.* Scaffolds with controlled release of pro-mineralization exosomes to promote craniofacial bone healing without cell transplantation. *Acta Biomater*. 2020;118:215-32. doi:10.1016/j.actbio.2020.09.052.
67. Gruber HE, Ingram JA, Davis DE, Hanley EN Jr. Increased cell senescence is associated with decreased cell proliferation in vivo in the degenerating human annulus. *Spine J*. 2009;9:210-5. doi:10.1016/j.spinee.2008.01.012.
68. Meng F, Henson R, Wehbe-Janek H, Ghoshal K, Jacob ST, Patel T. MicroRNA-21 regulates expression of the PTEN

- tumor suppressor gene in human hepatocellular cancer. *Gastroenterology*. 2007;133:647-58. doi:10.1053/j.gastro.2007.05.022.
69. Wu Y, Song Y, Xiong Y, Wang X, Xu K, Han B, *et al*. MicroRNA-21 (Mir-21) promotes cell growth and invasion by repressing tumor suppressor PTEN in colorectal cancer. *Cell Physiol Biochem*. 2017;43:945-58. doi:10.1159/000481648.
  70. Cao LQ, Yang XW, Chen YB, Zhang DW, Jiang XF, Xue P. Exosomal miR-21 regulates the TETs/PTENp1/PTEN pathway to promote hepatocellular carcinoma growth. *Mol Cancer*. 2019;18:148. doi:10.1186/s12943-019-1075-2.
  71. Liu H, Huang X, Liu X, Xiao S, Zhang Y, Xiang T, *et al*. miR-21 promotes human nucleus pulposus cell proliferation through PTEN/AKT signaling. *Int J Mol Sci*. 2014;15:4007-18. doi:10.3390/ijms15034007.
  72. Henriksson HB, Svala E, Skioldebrand E, Lindahl A, Brisby H. Support of concept that migrating progenitor cells from stem cell niches contribute to normal regeneration of the adult mammal intervertebral disc: a descriptive study in the New Zealand white rabbit. *Spine*. 2012;37:722-32. doi:10.1097/BRS.0b013e318231c2f7.
  73. Qu F, Guilak F, Mauck RL. Cell migration: implications for repair and regeneration in joint disease. *Nat Rev Rheumatol*. 2019;15:167-79. doi:10.1038/s41584-018-0151-0.
  74. Wangler S, Peroglio M, Menzel U, Benneker LM, Haglund L, Sakai D, *et al*. Mesenchymal stem cell homing into intervertebral discs enhances the Tie2-positive progenitor cell population, prevents cell death, and induces a proliferative response. *Spine*. 2019;44:1613-22. doi:10.1097/BRS.00000000000003150.
  75. Gao P, Wang D, Liu M, Chen S, Yang Z, Zhang J, *et al*. DNA methylation-mediated repression of exosomal miR-652-5p expression promotes oesophageal squamous cell carcinoma aggressiveness by targeting PARG and VEGF pathways. *PLoS Genet*. 2020;16:e1008592. doi:10.1371/journal.pgen.1008592.
  76. Wu L, Yuan W, Chen J, Zhou Z, Shu Y, Ji J, *et al*. Increased miR-214 expression suppresses cell migration and proliferation in Hirschsprung disease by interacting with PLAGL2. *Pediatr Res*. 2019;86:460-70. doi:10.1038/s41390-019-0324-9.
  77. Wang C, Yu X, Yan Y, Yang W, Zhang S, Xiang Y, *et al*. Tumor necrosis factor- $\alpha$ : a key contributor to intervertebral disc degeneration. *Acta Biochim Biophys Sin (Shanghai)*. 2017;49:1-13. doi:10.1093/abbs/gmw112.
  78. Cannell IG, Kong YW, Bushell M. How do microRNAs regulate gene expression? *Biochem Soc Trans*. 2008;36:1224-31. doi:10.1042/BST0361224.
  79. Ambros V. The functions of animal microRNAs. *Nature*. 2004;431:350-5. doi:10.1038/nature02871.
  80. Cazzanelli P, Wuertz-Kozak K. MicroRNAs in intervertebral disc degeneration, apoptosis, inflammation, and mechanobiology. *Int J Mol Sci*. 2020;21:3601. doi:10.3390/ijms21103601.
  81. Minogue BM, Richardson SM, Zeef LA, Freemont AJ, Hoyland JA. Transcriptional profiling of bovine intervertebral disc cells: implications for identification of normal and degenerate human intervertebral disc cell phenotypes. *Arthritis Res Ther*. 2010;12:R22. doi:10.1186/ar2929.
  82. Chen ZH, Jin SH, Wang MY, Jin XL, Lv C, Deng YF, *et al*. Enhanced NLRP3, caspase-1, and IL-1 $\beta$  levels in degenerate human intervertebral disc and their association with the grades of disc degeneration. *Anat Rec (Hoboken)*. 2015;298:720-6. doi:10.1002/ar.23059.
  83. Deng X, Zhao F, Kang B, Zhang X. Elevated interleukin-6 expression levels are associated with intervertebral disc degeneration. *Exp Ther Med*. 2016;11:1425-32. doi:10.3892/etm.2016.3079.
  84. Li ZQ, Kong L, Liu C, Xu HG. Human bone marrow mesenchymal stem cell-derived exosomes attenuate IL-1 $\beta$ -induced annulus fibrosus cell damage. *Am J Med Sci*. 2020;360:693-700. doi:10.1016/j.amjms.2020.07.025.
  85. Le Maitre CL, Freemont AJ, Hoyland JA. The role of interleukin-1 in the pathogenesis of human intervertebral disc degeneration. *Arthritis Res Ther*. 2005;7:R732-45. doi:10.1186/ar1732.
  86. Johnson ZI, Schoepflin ZR, Choi H, Shapiro IM, Risbud MV. Disc in flames: roles of TNF- $\alpha$  and IL-1 $\beta$  in intervertebral disc degeneration. *Eur Cell Mater*. 2015;30:104-16. doi:10.22203/eCM.v030a08.
  87. Le Maitre CL, Hoyland JA, Freemont AJ. Catabolic cytokine expression in degenerate and herniated human intervertebral discs: IL-1beta and TNFalpha expression profile. *Arthritis Res Ther*. 2007;9:R77. doi:10.1186/ar2275.
  88. Wang Y, Che M, Xin J, Zheng Z, Li J, Zhang S. The role of IL-1 $\beta$  and TNF- $\alpha$  in intervertebral disc degeneration. *Biomed Pharmacother*. 2020;131:110660. doi:10.1016/j.biopha.2020.110660.
  89. Bron JL, Helder MN, Meisel HJ, Van Royen BJ, Smit TH. Repair, regenerative and supportive therapies of the annulus fibrosus: achievements and challenges. *Eur Spine J*. 2009;18:301-13. doi:10.1007/s00586-008-0856-x.
  90. Bowles RD, Setton LA. Biomaterials for intervertebral disc regeneration and repair. *Biomaterials*. 2017;129:54-67. doi:10.1016/j.biomaterials.2017.03.013.
  91. D'Este M, Eglin D, Alini M. Lessons to be learned and future directions for intervertebral disc biomaterials. *Acta Biomater*. 2018;78:13-22. doi:10.1016/j.actbio.2018.08.004.
  92. Long RG, Torre OM, Hom WW, Assael DJ, Iatridis JC. Design requirements for annulus fibrosus repair: review of forces, displacements, and material properties of the intervertebral disk and a summary of candidate hydrogels for repair. *J Biomech Eng*. 2016;138:021007. doi:10.1115/1.4032353.
  93. DiStefano TJ, Shmukler JO, Dianas G, Iatridis JC. The functional role of interface tissue engineering in annulus fibrosus repair: bridging mechanisms of hydrogel integration with regenerative outcomes. *ACS Biomater Sci Eng*. 2020;6:6556-86. doi:10.1021/acsbomaterials.0c01320.
  94. Li X, Sun Q, Li Q, Kawazoe N, Chen G. Functional hydrogels with tunable structures and properties for tissue engineering applications. *Front Chem*. 2018;6:499. doi:10.3389/fchem.2018.00499.
  95. Mantha S, Pillai S, Khayambashi P, Upadhyay A, Zhang Y, Tao O, *et al*. Smart hydrogels in tissue engineering and regenerative medicine. *Materials (Basel)*. 2019;12:3323. doi:10.3390/ma12203323.

96. Anseth KS, Metters AT, Bryant SJ, Martens PJ, Elisseeff JH, Bowman CN. In situ forming degradable networks and their application in tissue engineering and drug delivery. *J Control Release*. 2002;78:199-209. doi:10.1016/s0168-3659(01)00500-4.
97. Liao H, Munoz-Pinto D, Qu X, Hou Y, Grunlan MA, Hahn MS. Influence of hydrogel mechanical properties and mesh size on vocal fold fibroblast extracellular matrix production and phenotype. *Acta Biomater*. 2008;4:1161-71. doi:10.1016/j.actbio.2008.04.013.
98. Guilak F, Ting-Beall HP, Baer AE, Trickey WR, Erickson GR, Setton LA. Viscoelastic properties of intervertebral disc cells. Identification of two biomechanically distinct cell populations. *Spine*. 1999;24:2475-83. doi:10.1097/00007632-199912010-00009.
99. Nachemson A. Intradiscal measurements of pH in patients with lumbar rhizopathies. *Acta Orthop Scand*. 1969;40:23-42. doi:10.3109/17453676908989482.
100. Ichimura K, Tsuji H, Matsui H, Makiyama N. Cell culture of the intervertebral disc of rats: factors influencing culture, proteoglycan, collagen, and deoxyribonucleic acid synthesis. *J Spinal Disord*. 1991;4:428-36. doi:10.1097/00002517-199112000-00004.
101. Rambhia KJ, Ma PX. Controlled drug release for tissue engineering. *J Control Release*. 2015;219:119-28. doi:10.1016/j.jconrel.2015.08.049.